Size-Dependent Structure of Silver Nanoparticles Under High Pressure

by

Kristie Jo Koski

B.S. (University of Wyoming) 2002

A dissertation submitted in partial satisfaction of the
requirements for the degree of
Doctor of Philosophy

in

Chemistry

in the

GRADUATE DIVISION
of the
UNIVERSITY of CALIFORNIA at BERKELEY

Committee in charge:

Professor A Paul Alivisatos, Chair
Professor Raymond Jeanloz
Professor Angelica Stacy

Fall 2008

Size-Dependent Structure of Silver Nanoparticles Under High Pressure

Kristie Jo Koski

Department of Chemistry
University of California, Berkeley

and

Materials Sciences Division
Lawrence Berkeley National Laboratory
University of California
Berkeley, California 94720

Fall 2008

This work was supported by the Director, Office of Energy Research, Office of Basic Energy Sciences, Materials Sciences Division, of the U.S. Department of Energy under Contract No. DE-AC02-05CH11231.

The dissertation of Kristie Jo Koski is approved:

Chair Date

Date

Date

University of California at Berkeley

Fall 2008

Size-Dependent Structure of Silver Nanoparticles Under High Pressure

Kristie Jo Koski

Abstract

Size-Dependent Structure of Silver Nanoparticles Under High Pressure

by

Kristie Jo Koski

Doctor of Philosophy in Chemistry

University of California at Berkeley

Professor A Paul Alivisatos, Chair

Silver noble metal nanoparticles, that have a diameter less than 10 nm, often possess multiply twinned grains allowing them to adopt shapes and atomic structures not observed in bulk materials. The properties exhibited by particles with multiply-twinned polycrystalline structures are often far different from those of single-crystalline particles and from the bulk. I will present experimental evidence that silver nanoparticles < 10 nm undergo a reversible structural transformation under hydrostatic pressures up to 10 GPa. Results for nanoparticles in the intermediate size range of 5 to 10 nm suggest a reversible linear pressure-dependent rhombohedral distortion which has not been previously observed in bulk silver. I propose a mechanism for this transition that considers the bond-length distribution in idealized multiply twinned icosahedral particles. At smaller sizes, results for 3.9 nm silver nanoparticles suggest a reversible linear orthorhombic distortion that continuously varies with hydrostatic pressure to 8GPa. This distortion is interpreted in the

context of idealized decahedral particles.

In addition, given these size-dependent measurements of silver nanoparticle compression with pressure, we have constructed a pressure calibration curve. Encapsulating these silver nanoparticles in hollow metal oxide nanospheres then allows us to measure the pressure inside a nanoshell using x-ray diffraction. We demonstrate the measurement of pressure gradients across nanoshells and show that these nanoshells have maximum resolved shear strengths on the order of 500 MPa to 1GPa.

Professor A Paul Alivisatos
Dissertation Committee Chair

Contents

List of Figures

List of Tables

Acknowledgements

I am grateful to my advisor, Professor A. Paul Alivisatos for the opportunity to pursue the exploratory work presented in this thesis and his guidance during my years in graduate school. His scientific curiosity and scientific inclinations have greatly influenced and motivated my own ways of doing research. I would like to acknowledge all the present and past members of the Alivisatos group, especially Noelle Kamp, Rachel K. Smith, Haitao Liu, Can Erdonmez, Yadong Yin, Andreu Cabot, Joey Luther, Jonathan S. Owen, Matt Sheldon, Bryce Sadtler, Steven Hughes, Josh Wittenberg, Alexander Mastroianni, Meredith McMurdo, Sassan Sheikholeslami, Richard Robinson, Haimei Zheng, Yue Wu, Gordana Dukovic, Emory Chan, Bjoern Reinhard, Jungwon Park, Young-Wook Jun, Jessy Baker, Charina Choi, Katie Lutker, Jesse Engel, Shelley Claridge, Trevor Ewers, Paul Trudeau, and Dr. Aihua Fu. I would like to acknowledge our administrative assistant, Rita Tidwell, for her many efforts to make life run more smoothly.

I am greatly indebted to Raymond Jeanloz for giving me the opportunity to sit in on his group meetings at which I was introduced to most of the crystallography and solid mechanics extensively used in this work. I would like to acknowledge the support and all of the Jeanloz group members, especially Brent Grocholski, Arianna Gleason, Dylan Spaulding, Ryan Stewart, Sergio Speziale, and Godwall.

I would also like to acknowledge the invaluable guidance, both computationally and personally, of Jeff Grossman and Richard Klein. Much of this work could not have been accomplished without the invaluable assistance from Martin Kunz, Jason Knight, Sander Caldwell, and Simon Clark.

Last, I am very grateful for the invaluable support, theoretical & experimental insights, countless hours of coding help, endless encouragement, and the heroic open-ocean rescue of Bryan Reed.

All high pressure x-ray diffraction studies presented herein were performed at beamline 12.2.2 of the Advanced Light Source (ALS) at Lawrence Berkeley National Laboratory. This work was supported in part by the Air Force Office of Scientific Research award No. FA9550-07-1-0334, in part by the Director of the Office of Science, Office of Basic Energy Sciences, U.S. Department of Energy under Contract No. DE-AC02-05CH1123, and in part under the auspices of the National Science Foundation by University of California Berkeley under Grant No. 0425914.

Symbols

Variables

ν	Poisson's Ratio
K_o	Bulk Modulus
E	Young's Modulus
Y	Yield Strength / Tensile Strength
a	Inner radii
P_a	Pressure inside sphere
b	Outer radii
P_b	Pressure outside sphere
σ_{ij}	Component of stress tensor
ϵ_{ij}	Component of strain tensor
τ_{max}	Maximum shear stress / Von Mises stress

Abbreviations

DAC	Diamond Anvil Cell
XRD	X-ray Diffraction
SAXS	Small Angle x-ray Scattering
TEM	Transmission Electron Microscopy
HRTEM	High Resolution Transmission Electron Microscopy
Ih	Icosahedral
Dh	Decahedral
FCC	Face centered cubic
BCO	Body centered orthorhombic
Ag	Silver
Pt	Platinum
Be	Beryllium
Co_3S_4	Cobalt Sulfide (Linnaeite)
CoO	Cobalt II Oxide
Fe_3O_4	Iron Oxide (Magnetite)

Chapter 1

Introduction

The chymists are a strange class of mortals, impelled by an almost insane impulse to seek their pleasure among smoke and vapour, soot and flame, poisons and poverty; yet among all these evils I seem to live so sweetly that may I die if I would change places with the Persian King.

Johann Joachim Becher Acta Laboratorii Chymica Monacensis, seu Physica Subterranea, (1669).

1.1 Motivation

Physically, a noble metal is one in which all of the d-bands of the electronic structure are filled (i.e. copper, silver, gold). They are well understood thermodynamically in terms of their P-V-T behavior. Noble metals are often used as x-ray diffraction calibrants.[1–3] Noble metals have been widely studied experimentally, computationally, and theoretically. They are fcc with low stacking fault energies so energetically they are closed-packed. Some of the first identified nanoparticles have been noble metals. They exist in nature[4]; and, not only that, but noble metal nanoparticles have been used for centuries. For example, going back 1000s of years, the Romans used Au nanoparticles to create red colored glass.

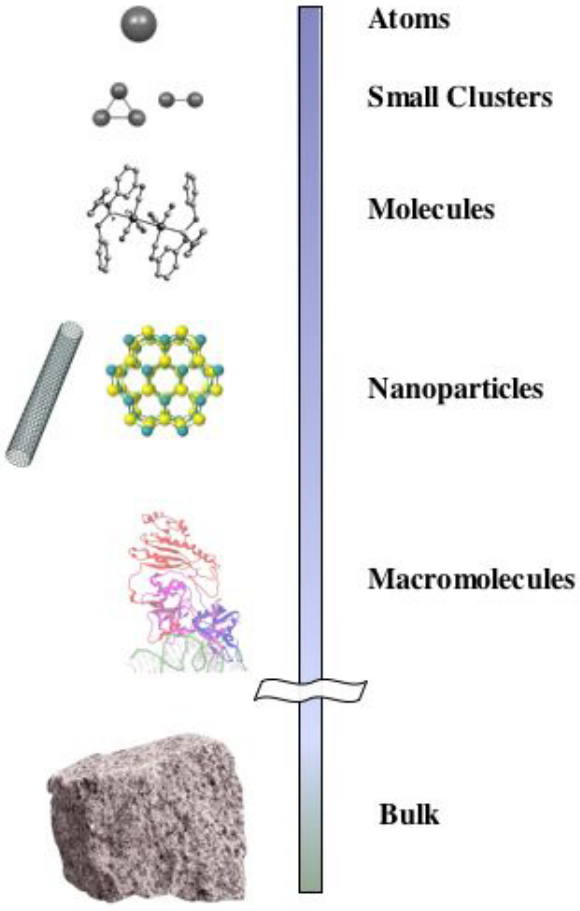

Figure 1.1: Scalebar of the size-scale relationship between clusters, nanoparticles, and bulk.

The "Aurum Potable" of the Swabian chemist, Paracelsus, which was a purple tonic meant as an alchemical cure-all, was simply a suspension of gold nanoparticles in water. Silver nanoparticles have often been cited for their anti-microbial properties and have even been useful in treating smelly socks.[5]

Nanoparticles exhibit unique thermodynamic trends because the decrease in the size of a solid leads to some interesting anomalies in its physical properties. For example, in 1954, Takagi first observed the decreased melting point of Pb, Sn, and Bi metal nanoparticles

using a variable intensity electron beam and electron diffraction.[6] In silver nanoparticles, the size dependence of the melting temperature has been clearly shown by Castro et al.[7] and Shyjumon et al.[8]

The pressure-dependent behavior in nanoparticles is equally striking. For example, phase transitions shift with size and pressure. Some classic examples of this are CdSe quantum dots which were found to have a size-dependent shift of their phase transition with pressure from between 2-3 GPa to upwards of upwards of 6 GPa depending upon the size of the nanoparticle.[9–11] The pressure driven phase transition of the γ to α in iron oxide nanoparticles has been found to increase with decreasing nanoparticle size from 24 GPa in bulk to 37 GPa in 3.2 nm nanoparticles.[12] Another remarkable trend with nanoparticles and pressure is that the bulk modulus can increase *o*r decrease with size.[12] The established reasons for this behavior are i) quantum confinement effects due to the small size of the nanoparticle and ii) nanoparticles have a high surface-to-volume ratio. Some of these quantum mediated effects arise because the characteristic dimensions of the nano-system are often comparable with other critical dimensions such as mean free paths, scattering lengths, or coherence lengths. Also, quantum confinement leads to discretized density of electronic states.[13] The consequence of having a small particle means that there is a greater amount of surface relative to the more bulk like material which tends to alter nanoparticle properties dramatically because of the consequentially high surface energies. Thermodynamically, we often refer to the free energy of a system. In a small system, the free energy of particle = free energy of bulk + free energy of surface. If the fraction of free energy that is surface energy increases then that alters things like phase equilibrium lines.

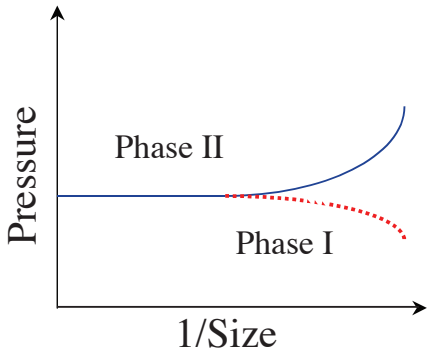

Figure 1.2: Nanoparticle phase transitions as a function of pressure shift with size. A pressure driven solid-solid phase transition can either decrease or increase with size.

I.e. since pressure is a derivative of the free energy, changes in the free energy functions have a huge impact on where phase transitions occur.

The primary question posed in this research is "What is the pressure dependent behavior in silver noble metal nanoparticles?" Our primary curiosity in asking this question, however, was to ultimately use encapsulated silver nanoparticles, as an x-ray diffraction calibrant, to measure the pressure inside of a hollow nanosphere.

Via the Kirkendall effect, Yin et al showed that it is possible to synthesize hollow nanospheres of metal oxide and metal sulfides.[14,15] In the Kirkendall effect, if the diffusion rates of two species are different there is a net flow of matter and also equal and opposite net flow of vacancies. When the vacancies become supersaturated they condense into voids in the fast diffusion species side.[16,17] In nanocrystals, this leads to hollow structures. These hollow nanospheres can be made from a variety of materials (Co_xO_y, Co_xS_y, Fe_xO_y, CdS, etc...)[14,15,18,19] A lot of interest exists in the behavior of hollow nanostructures under pressure.[13] We foresaw encapsulation of silver, or other noble metal nanoparticle, as a unique method of probing the pressure dependent behavior and mechanical properties of hollow

nanospheres.

Many of the chapters that follow have been published or are currently being prepared for publication. Hence, the figures, references, experimental methods, introduction, and conclusions are local to each chapter.

1.2 Dissertation Outline

This dissertation focuses on the structural behavior of silver nanoparticles < 10 nm as well as the application of silver nanoparticles toward measuring the mechanical properties of hollow nanospheres. The organization of this work is as follows: In Chapter 2, I introduce the predominant morphologies of silver nanoparticles as a function of nanoparticle size and discuss the resulting x-ray diffraction behavior. In Chapter 3, I present x-ray diffraction measurements of the structural distortion of silver nanoparticles in the intermediate size range of 5–10 nm under high pressure. In this work, we found that silver nanoparticles in this intermediate size range undergo a noncubic distortion with pressure. We found that this distortion was consistent with a rhombohedral distortion. I proposed a mechanism for this distortion based on the bond length distribution of an idealized icosahedral particle. In Chapter 4, I present a special case of x-ray diffraction measurements of 3.9 nm silver nanoparticles and the noncubic structural distortion in those particles. We interpret this distortion as an orthorhombic distortion assuming an idealized decahedral structure of these particles. Chapter 5 presents the encapsulation of silver nanoparticles in metal oxide hollow nanospheres and measurements of the pressure gradients across the hollow nanoshells using the encapsulated silver. In Chapter 6, I present a similar case, not using silver nanoparticles,

wherein we measure the pressure inside a hollow nanosphere with a multi-branched platinum particle and show very large stress gradients can occur inside the hollow nanosphere due to the shape of the platinum particle. Finally, in Chapter 7, for the sake of the reader, I present some experimental details shared by all these experiments.

Chapter 2

Background

I can hardly doubt that when we have some control of the arrangement of things on a small scale we will get an enormously greater range of possible properties that substances can have.

R. P. Feynman

2.1 Multiply twinned silver nanoparticles

As the size of a solid is decreased, its equilibrium structure reflects a minimum of the total free energy of the particle, with both surface energy and bulk energy terms included.[20] With an increasing ratio of surface atoms, the structures and properties can dramatically vary from those of the stable bulk solid structure. A unique consequence of this is that small particles < 10 nm, a size wherein a great number of the total atoms are on the surface, can adopt unique morphologies and structures that have never been observed in the bulk.[20–25] Many of the metals that assume fcc crystallography in the bulk adopt structures, possessing fivefold symmetry, that are polycrystalline and multiply twinned.

These structure are often ideally described as decahedra and icosahedra. The basic rationale for these types of structures is the surface energy is lowered at the expense of an internal strain through the creation of twin boundaries, specifically twin pentajunctions,which are impossible in an unstrained cubic crystal, which make it possible for most or all exposed surfaces to be {111} faces which have particularly low surface energy in fcc materials. The net reduction in surface energies at these smaller sizes thus outweighs the energy cost of internal strain and twinning.

Multiply twinned nanoparticles possessing these geometries were first identified by Ino in 1969, long before the days of high resolution TEM.[21,25,26] In this early work, it was established that these crystal structures would be adopted by small particles because the energy cost of the internal strain is offset by a favorable rearrangement of surface atoms. In other words, the interplay of surface energy and strain energy is such that it is more favorable to have this distorted, polycrystalline particle of unique morphology than a spherical, face-centered cubic particle.

Not all fcc metals will form multiply-twinned structures. The formation of multiply-twinned particles depends on the energetics as well as the growth kinetics and the substrate the particles are grown on. Icosahedral and decahedral shapes are seen in Au, Ag, Ni, and Pd.[27] In Fe, Co, Cu, and Pb shapes that are observed tend to be Dh or truncations off the cuboctahedral shape. In Pt, the shape is cuboctahedral single twinned with no Ih or Dh formed.[27]

Figure 2.1 shows the structures characteristically identified in multiply-twinned noble metal nanoparticles and in particular, silver noble metal nanoparticles. The deca-

hedral structure tends to be adopted at smaller sizes and the icosahedral at intermediate sizes. A regular decahedron is never observed and the isodecahedron is rarely found. The most commonly observed Dh structure is the Marks decahedron (not shown), which is a truncated decahedron with extra <111> facets that give the particle a star-like appearance, or a faceted decahedron as shown in Fig. 2.1 as described by Ino which has exposed <100> faces.[21,27] The fcc spherical non-twinned structure is seen at much larger sizes of particle.

Multiply twinned particles have discrete symmetry of non-crystallographic point groups.[20,22,23,28] When constructed from perfect single-crystal units, neither atomic arrangement of the Dh or the Ih is completely space-filling. Thus, some form of internal distortion must be incorporated. Some examples of these are a homogenous elastic strain [29], an inhomogeneous strain [28,30], dislocations [23,28,31,32] or a crystal structure modification.[28,33,34]

The icosahedron comprises 20 grains, each of which is a not-quite-regular tetrahedron in which each unit cell has a rhombohedral distortion that (in the ideal case) has magnitude $\epsilon = 0.0261$ (see Equation 3.1 for the definition of ϵ). Each such tetrahedron has one {111} face on the outer surface, while the other three {111} faces are twin boundaries separating one grain from the next. These 30 twin boundaries come together in 12 five-fold junctions corresponding to the 30 edges and 12 vertices of the icosahedron. The rhombohedral distortion is required so that the structure fills space in three dimensions (a twin pentajunction in an undistorted fcc crystal being geometrically impossible).[35,36]

The decahedron, similarly, has 5 grains, each of which is a tetrahedron with body-centered orthorhombic crystal structure. This structure has one pentajunction line, 5 twin boundaries, and 10 exposed {111} surfaces. Because of the high energy of acute-angled

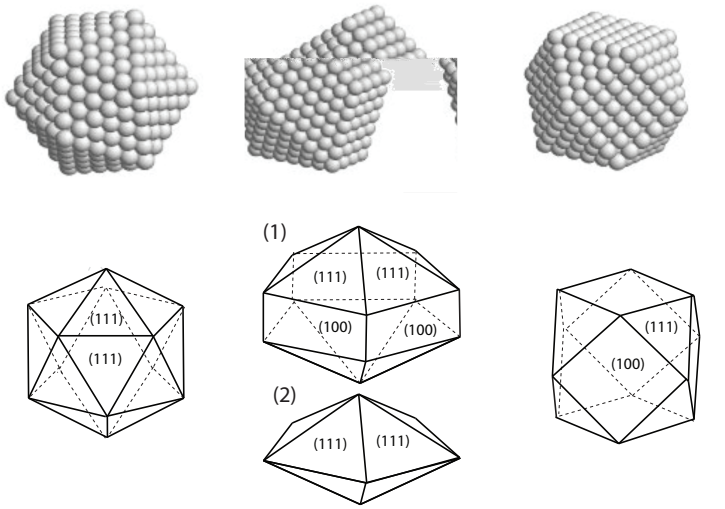

Figure 2.1: Structures characteristically found in multiply-twinned noble metal nanoparticles. The exposed lattice planes are labeled. Note the greater fraction of the low-energy {111} faces in the Ih and Dh structures over the cubocatahedron.

edges, the outer edges typically either round off or form facets, such as the {100} facets in the truncated decahedron of Figure 2.1. The Dh structure is less constrained than the Ih structure, and we introduce a dimensionless free parameter γ (defined in Equation 4.1) that characterizes the degree of stretch along the pentajunction line. Yang [35] found that a distortion corresponding to $\gamma = 0.051$ yields close-packed exposed surfaces, but there is little a priori reason for insisting on this condition.

2.2 X-ray diffraction of multiply-twinned structures

2.2.1 Relationship between FCC, Orthorhombic, and Rhombohedral crystal structures.

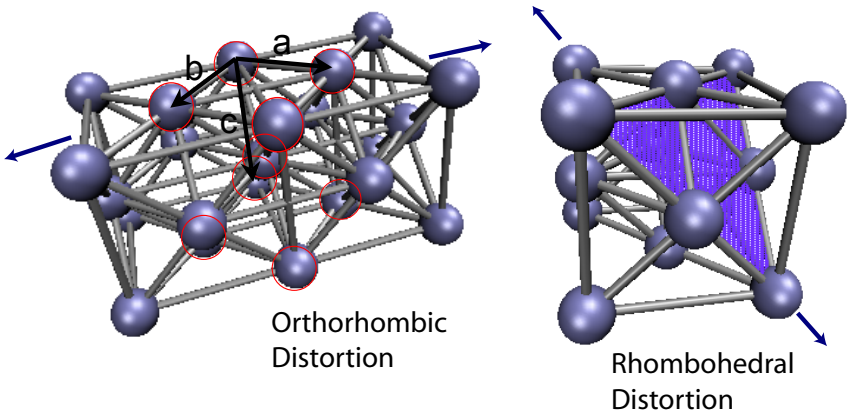

Figure 2.2: Pictorial descrption of a rhombohedral and orthorhombic distortion given an fcc unit cell. A description is given in the text.

As mentioned above, these decahedral and icosahedral crystal structures are adopted because the energy cost of the internal strain is offset by a favorable rearrangement of surface atoms. In the decahedral particle (pentagonal dipyramid or truncated decahedron), as was shown in a hard sphere model by Bagley, the atomic lattice assumes a body-centered orthorhombic unit cell.[33] In the icosahedral particle, the atomic structure is the result of a uniaxial strain along a [111] direction in the fcc crystal to stabilize the atoms in the icosahedron. This is a rhombohedral type of distortion. [35]

Resulting multiply twinned structures, decahedral and icosahedral, consist of structures that can be thought of as distortions off of an fcc lattice. In order to illustrate what is meant by these types of distortions, I give a pictorial description in Figure 2.2. A rhombohedral distortion from an fcc unit cell can be illustrated as taking opposite atoms on the corners of the fcc basis and pulling on those atoms in opposite direction. This will cause a shearing of the unit cell which is basically a stretch along the [111] lattice direction. An orthorhombic distortion is more elusive pictorially. An easily visualized orthorhombic

$(h_O k_O l_O)$	d_O [Å]	d_O/d_{fcc}	(hkl)	d_{fcc}	$(h_R k_R l_R)$	d_R [Å]	d_R/d_{fcc}
(011)			(111)		(111)	2.30	$\frac{1}{\sqrt{3+12\epsilon+12\epsilon^2}}$
	2.41	$\frac{1}{\sqrt{0.5278+\frac{1}{(1+\gamma)^2}}}$					
$(01\bar{1})$			$(11\bar{1})$		(001)		
				2.36		2.46	$\frac{1}{\sqrt{3-4\epsilon+4\epsilon^2}}$
(101)	2.34	0.80902	$(1\bar{1}1)$		(010)		
$(\bar{1}01)$			$(\bar{1}11)$		(100)		
(110)		$\frac{1}{\sqrt{1+\frac{1}{(1+\gamma)^2}}}$	(200)		(011)		
$(\bar{1}10)$	1.90		(020)		(101)		$\frac{1}{\sqrt{4+8\epsilon^2}}$
				2.04		2.09	
(002)	1.99	0.68819	(002)		(110)		
(200)	1.45	0.5	$(2\bar{2}0)$		$(\bar{1}10)$		$\frac{1}{2\sqrt{4-4\epsilon+4\epsilon^2}}$
$(11\bar{2})$			$(20\bar{2})$		$(\bar{1}01)$	1.52	
$(\bar{1}1\bar{2})$		$\frac{1}{\sqrt{3.11146+\frac{1}{(1+\gamma)^2}}}$	$(02\bar{2})$		$(0\bar{1}1)$		
	1.44			1.45			
$(\bar{1}12)$			(022)		(211)		
(112)			(202)		(121)		
						1.44	$\frac{1}{2\sqrt{2+4\epsilon+6\epsilon^2}}$
(020)	1.52	$\frac{1+\gamma}{2}$	(220)		(112)		
(103)			$(1\bar{1}3)$		(120)		
$(\bar{1}03)$	1.20	0.417021	$(\bar{1}13)$		(210)		$\frac{1}{\sqrt{11-4\epsilon+20\epsilon^2 2}}$
						1.27	
$(12\bar{1})$			$(31\bar{1})$		(012)		
$(\bar{1}2\bar{1})$			$(13\bar{1})$		(102)		
	1.27	$\frac{1}{\sqrt{1.5278+\frac{4}{(1+\gamma)^2}}}$					
(121)			(311)		(122)		
$(\bar{1}21)$			(131)		(212)		
				1.23		1.22	$\frac{1}{\sqrt{11+28\epsilon+36\epsilon^2}}$
(013)			(113)		(221)		
	1.22	$\frac{1}{\sqrt{4.75022+\frac{1}{(1+\gamma)^2}}}$					
$(0\bar{1}3)$			$(\bar{1}\bar{1}3)$		$(11\bar{1})$		
$(\bar{2}11)$			$(\bar{1}3\bar{1})$		$(1\bar{1}1)$	1.29	$\frac{1}{\sqrt{11-20\epsilon+12\epsilon^2}}$
$(21\bar{1})$			$(3\bar{1}\bar{1})$		$(\bar{1}11)$		
(211)		$\frac{1}{\sqrt{2.5278+\frac{1}{(1+\gamma)^2}}}$	$(3\bar{1}1)$		(021)		
	1.24						
(211)			$(3\bar{1}1)$		(021)	1.27	
$(\bar{2}11)$			$(\bar{1}31)$		(201)		$\frac{1}{\sqrt{11-4\epsilon+20\epsilon^2}}$

Table 2.1: Table of the general rhombohedral, fcc, and orthorhombic correspondences adapted from the less general case of Ref. 35. ϵ and γ are distortions toward each phase. The relative d-spacing value has been added to show how this alters with an orthorhombic or rhombohedral distortion (assuming $\gamma = 0.051$ and $\epsilon = 0.0261$).

distortion is the special case of the tetragonal distortion wherein taking opposite faces of the fcc unit cell and pulling them in opposite directions yields a tetragonal distortion in a [100] direction. It's more difficult to visualize an orthorhombic distortion which is a stretch along the [110] direction as in the decahedra. Fig. 2.2, illustrates an orthorhombic distortion. First, we take the fcc unit cell and identify a body centered tetragonal unit cell as 45^o rotated cell with the aspect ratio $[1, 1, \sqrt{2}]$ (the 9 red atoms). Next we compress the c direction (fcc [001], bco [001]) to c = 1.376a instead of the 1.414 in fcc structure so that the tetrahedra fit together. Now the cell is strained in the b direction (fcc $[1, \bar{1}, 0]$, bco [010]) by some variable amount, γ. The unit cell vector, a, thus ends up being parallel to the outer edge, b is parallel to the pentajunction line, and c is parallel to a line linking the center of a decahedron to the center of an outer edge.

Yang [35] derived the correspondence relationships between the (hkl) of the face centered cubic lattice, the body-centered orthorhombic lattice, and the rhombohedral lattice assuming close-packing along the faces and close-packing along the twins respectively. In Table 2.1, I show those correspondence relationships between orthorhombic, rhombohedral, and FCC crystal structures assuming the general case where the close-packing is not known but the amount of distortion in each case is given by ϵ for rhombohedral and γ for orthorhombic. Further explanations of how this information can be applied as well as derived can be found later in this text (see Chapter 3 and Chapter 4). The values of the theoretical d-spacing for each hkl for each structure in this table as found from the bulk value of silver (assuming $\gamma = 0.051$ and $\epsilon = 0.0261$) are presented to give an idea of how much each lattice distortion causes the peaks to shifts for any given distortion. The nearest

neighbor distances from these correspondence can be found in Yang et al.[35]

Figure 2.3 illustrates a hypothetical x-ray diffraction pattern for bulk silver as determined from the correspondence relationships above. This figure shows the splittings of each peak if the lattice was rhombohedral or body-centered orthorhombic rather than fcc. The splittings are given assuming a positive orthorhombic or rhombohedral distortion. It is important to note that, experimentally, we determined that either of these distortions tends to be negative. The result then, for example, in a negative rhombohedral type distortion, would be a shift of the shoulder of the {111} peak to lower d-spacing values.

This is just an effective way to picture what the x-ray diffraction pattern would look like given an orthorhombic distortion or a rhombohedral distortion. It serves as an aid for information given later in the body of this work.

As can be seen from this plot, in an orthorhombic distortion, the {111} peak from an undistorted fcc structure splits into two equal intensity peaks, the {200} separates into two peaks with one twice as intense as the other, and the {220} peak splits into three peaks with one four times as intense as the other two. The {311} splits into four peaks with two half the intensity of the other two. This is also accompanied by a concomitant shift of the d spacings.[35] The d-spacing shift isn't displayed in the figure, this however, can be found in Table 2.1 which shows the d-spacings, hypothetically, given each crystal structure for silver.

In a rhombohedral crystal, the {111} peak separates into two peaks with one a third the intensity of the other. The {200} peak remains unchanged, and the {220} peak splits into a doublet of equal intensity. The {311} peak splits into a triplet with one twice the intensity of the other two.[35]

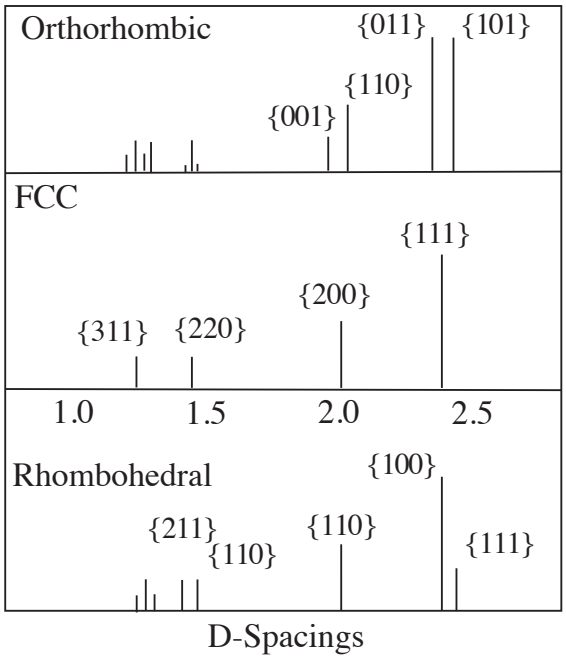

Figure 2.3: Correspondence relationships between orthorhombic ,FCC, and rhombohedral crystal structures for silver pertaining to Table 2.1.

The resulting multiply-twinned nanoparticles, icosahedral and decahedral, will have different exposed crystal faces depending upon the nanoparticle morphology. Figure 2.1 shows the common multiply-twinned morphologies labeled with their exposed lattice planes. It is interesting to note that an icosahedron and a pentagonal decahedron have only exposed {111} faces. The more commonly observed, truncated decahedron has exposed {100} facets in addition to the {111} facets the comprise the pentajunction.

2.3 Growth mechanisms of silver Ih and Dh particles

Experimentally, the observed structure of a silver particle is the result of the competition between thermodynamic and kinetic factors. Table 2.2 presents the mean

Mean Diameter [nm]	N_{atoms}	Structure
Ag < 1nm	$N_{atoms} < 100$	Ih, Dh, fcc, amorphous
1 nm < Ag < 4 nm	$80 < N_{atoms} < 1000$	Decahedral
4 nm < Ag < 11 nm	$1000 < N_{atoms} < 25{,}000$	Icosahedral
Ag > 11nm	$N_{atoms} > 25{,}000$	fcc

Table 2.2: Table of silver nanoparticle predominant ideal structure as determined by the nanoparticle size and, roughly, the number of Ag atoms.

diameter and the dominant structure that best describes silver nanoparticles identified in those size ranges.[24,37–43] This work presents experimental investigations of nanoparticles in the size ranges favoring predominantly icosahedra and predominantly decahedra.

Experiments and theoretical predictions of the structure of silver nanoparticles do not agree (i.e. the table shown above is not found in theoretical works). Calculations by Boletto et al. found that Ag adopts an icosahedral structure for clusters smaller than 300 atoms ($\sim$ 2 nm), a decahedral structure for 300–20,000 atoms (about 2 nm to 8 nm), and an fcc structure at much larger sizes. This is in sharp contrast to aforementioned experiments.[45–47] However, further calculations by Balleto et al. have explained this disagreement in terms of a solid state growth model as a kinetic trapping effect, where during the formation of the silver cluster, the structures become trapped in their small sized morphology leading to the growth of metastable structures such as icosahedral silver.[43,47,48]

These results suggest that Ag should be Dh for both small and intermediate sizes. The conclusion though is that at the smaller sizes, the icosahedral structure gets stuck and is built upon layer by layer with hexagonal pieces of silver clusters. Thus in the intermediate size range we get icosahedra. Koga et. al have made some convincing measurements of the statistics of multiply-twinned gold particle growth using inert gas aggregation. This revealed

that both Dh and Ih morphologies grow at small sizes and that indeed the hypothesis of Baletto et al may be relevant for the formation gold multiply-twinned particles.[49]

Whether or not there is a discrete transition between decahedra and icosahedra is as yet unclear and seems to be weighted by the kinetic and thermodynamic factors of the experiment. Theoretical studies suggest that the transition is not discrete or instantaneous.[43,47,48] In experimental investigations, an ensemble of Dh and Ih morphologies is produced with one being more dominant at any given size scale.[24,41,49]

2.4 Multiply-twinned nanoparticles under pressure

These multiply twinned structures are intrinsically strained. Addition of pressure (an external stress) should have a large impact in the crystallographic nature and structural behavior of these particles. Thermodynamically, it has been shown that with temperature, multiply-twinned particles can undergo a phase transition to fcc structure by Sato et al.[44] It remained an interesting question how these structures respond to pressure.

Before these studies, only one other high pressure crystallographic experimental investigation on Ag noble metal nanoparticles had been pursued to the knowledge of the author. Gu et al measured the compressibility of commercial silver (10 nm) and commercial gold nanoparticles (30 nm) via x-ray diffraction. They found that Ag and Au nanoparticles demonstrated a bulk modulus much greater than that of the bulk.[50] They found no evidence of any crystallographic distortion with pressure in their investigation unlike investigations that will be covered in this work. It's likely that all of their nanoparticle studies were of agglomerates hence there was no separation of nanoscale and bulk effects. The potential

for agglomeration is important. In measurements of one particular sample, we did see agglomeration, with XRD grain sizes clearly larger than the initial particles sizes. In this case, we did not see any distortion. It is important to mention that in silver encapsulated with a hollow nanosphere, as in Chapter 5, we do see structural distortions.

The only computational investigations on the behavior of noble metal clusters with pressure was done by Calvo and Doye[51] where they looked at three structures (Ih, Dh, and de Wulfe polyhedra) and predicted the size versus pressure-dependent phase transitions for each structure for these clusters. The clusters in these studies were less than 100 atoms which for silver is approximately <1 nm.

2.5 Bulk silver

Bulk silver, like so many other noble metals, adopts a face-centered cubic structure. Under pressure, no phase transitions or distortions have been identified in bulk silver up to 200 GPa using shock compression methods [52] and up to 146 GPa using diamond anvil cell compression techniques.[2]

The bulk modulus and the pressure derivative of the bulk modulus of silver in the bulk has been measured by many sources using many different methods as listed in Table 2.3. This is by no means a complete table of all experimental results available. It is interesting to note the spread in the values of these elastic constants from silver from these various experimental methods especially in the zero-pressure bulk modulus as measured from ultrasonic techniques.

	Ko (GPa)	Ko'	Technique	Equation	Reference
Ag	105.7	5.4	Shock wave	BM3	Ref. 53
	98	5.5	Shock wave	Vinet	Ref. 53
	104.5	6.0	Shock wave	Vinet	Ref. 52
	116.3	5.9	XRD	BM3	Ref. 54
	116	4.7	XRD	BM3	Ref. 55
	89.1	5.9	XRD	Vinet	Ref. 2
	100.0	6.0	XRD	BM3	Ref. 56
	108.5	7.0	XRD	BM2	Ref. 57
	109.8	6.1	XRD	BM3	Ref. 57
	120.9	2.5	Mechanical compression	BM2	Ref. 58
	103.6	6.2	Ultrasonics	(BM2)	Ref. 59
	99.9	6.1	Ultrasonics		Ref. 60
	97.4	4.3	Ultrasonics		Ref. 61
	139	4	XRD	BM2	Ref. 50*
	121	8.3	XRD	BM3	Ref. 50*

Table 2.3: Table of the bulk moduli and pressure derivative of the bulk moduli of silver given by different references using different experimental techniques. Asterisks are for silver nanoparticles.

BM2 and BM3 are the second order and third order Birch Murnaghan equation of state respectively as used to determine the bulk modulus in the experiment presented in Table 2.3. Where the Birch-Murnaghan equation is given by:

$$P = \frac{3}{2} Ko \left[\left(\left(\frac{V_o}{V} \right)^{\frac{7}{3}} - \left(\frac{V_o}{V} \right)^{\frac{5}{3}} \right) \right] \tag{2.1}$$

for BM2 and:

$$P = \frac{3}{2} Ko \left[\left(\left(\frac{V_o}{V} \right)^{\frac{7}{3}} - \left(\frac{V_o}{V} \right)^{\frac{5}{3}} \right) \right] \left[1 + \frac{3}{4} (K'_o - 4) \left(\left(\frac{V_o}{V} \right)^{\frac{2}{3}} - 1 \right) \right] \tag{2.2}$$

for BM3 and the Vinet equation of state by:

$$P = 3K_o \left(\frac{V_o}{V}\right)^{\frac{2}{3}} \left[1 - \left(\frac{V}{V_o}\right)^{\frac{1}{3}}\right] \exp\left(\frac{3}{2}(K'_o - 1)\left[1 - \left(\frac{V}{V_o}\right)^{\frac{1}{3}}\right]\right) \tag{2.3}$$

Silver is an ideal x-ray diffraction calibrant because it has such a high compressibility (low bulk modulus).[2,52–58] To show how bulk silver compares in compressibility to other noble metals, a periodic table of bulk moduli of elements collected from several sources by Noelle M. Kamp is given in Fig. 2.5. Noble metals, not just those of full d bands but also those traditionally called noble metals (Ni, Cu, Ru, Rh, Pd, Ag, Re, Os, Ir, Pt, Au, Hg) are grayed out. To us, this indicated that silver was the ideal material to embed in a hollow nanosphere to measure the mechanical properties of nanomaterials as will be discussed in Chapter 5.

2.5.1 Hollow Nanospheres

As mentioned in Chapter 1, we are able to synthesize hollow nanospheres of metal oxide and metal sulfides.[14,15] Figure 2.4 shows the synthetic route by which formation of nanoshells occurs via the Kirkendall effect as well as how we encapsulate noble metal nanoparticles like silver inside the nanoshell. These hollow nanospheres can be made from a variety of materials but those presented in this work are: Co_xO_y, Co_xS_y, and Fe_xO_y. The basic route of formation is that a metal nanoparticle of cobalt or iron is synthesized with or without a metal core and then exposed to oxygen, sulfur, or selenium. The result is a hollow sphere of metal chalcogenide encapsulating a metal nanoparticle with a void space in between. Using the encapsulated metal nanoparticle is a unique way of probing the otherwise inaccessible void region of the hollow nanosphere.

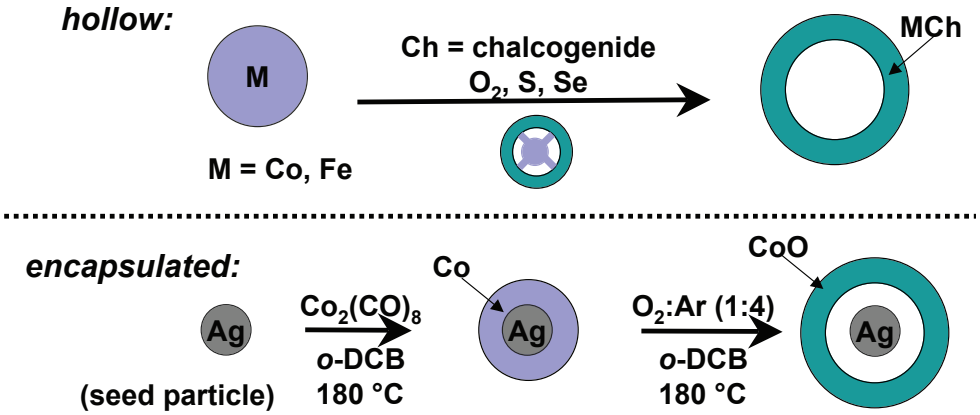

Figure 2.4: Formation of hollow nanospheres and encapsulation of metal nanoparticles in hollow nanospheres using the Kirkendall effect.[14,16]

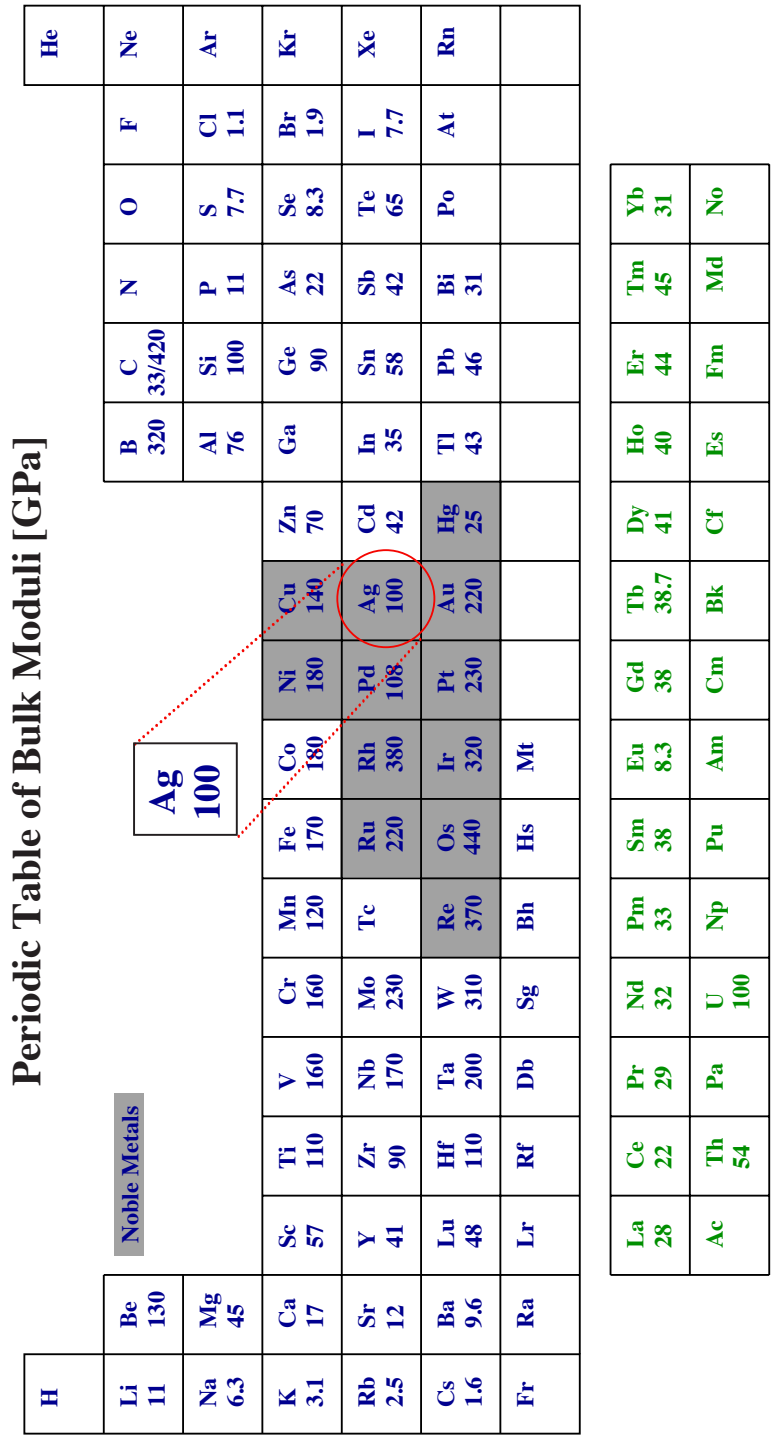

Figure 2.5: Periodic table of bulk moduli of the elements. Grayed boxes are the noble metals. Ag is highly compressible as compared to other noble metals.

Chapter 3

Structural Distortions in 5 – 10 nm Silver Nanoparticles Under High Pressure

Reproduced in part with permission from "K. J. Koski, N. M. Kamp, R. K. Smith, M. Kunz, J. K. Knight and A. P. Alivisatos, "Structural distortions in 510 nm silver nanoparticles under high pressure" *Physical Review B* **78**, 165410, 2008".

3.1 Abstract

We present experimental evidence that silver nanoparticles in the size range of 5 – 10 nm undergo a reversible structural transformation under hydrostatic pressures up to 10 GPa. We have used x-ray diffraction with a synchrotron light source to investigate pressure-dependent and size-dependent trends in the crystal structure of silver nanoparticles

in a hydrostatic medium compressed in a diamond-anvil cell. Results suggest a reversible linear pressure-dependent rhombohedral distortion which has not been previously observed in bulk silver. We propose a mechanism for this transition that considers the bond-length distribution in idealized multiply twinned icosahedral particles. To further support this hypothesis, we also show that similar measurements of single-crystal platinum nanoparticles reveal no such distortions.

3.2 Introduction

Noble metal nanoparticles, such as Ag, Cu, Pd, and Au, at sizes of <10 nm often possess multiply twinned grains that allow them to adopt shapes and atomic structures not existing in bulk materials.[62,63] The properties exhibited by particles with multiply twinned polycrystalline structures are often far different from those of single-crystalline particles or from the bulk. The exposure of specific surfaces and the presence of particular grain boundaries facilitates interesting mechanical and chemical behaviors and alters the surface properties.[62,64,65] The argument has been made that these crystal structures are adopted by clusters because the energy cost of the internal strain is offset by a favorable rearrangement of surface atoms.[24] The question then arises, what happens to the internal strain and the atomic structure if one puts an external stress, such as pressure, onto these types of structures?

These intermediate-sized clusters frequently feature five fold twin junctions which yield structures that are ideally described as decahedral (Dh) or icosahedral (Ih).[20,63] The Dh and Ih are constructed of irregular tetrahedral grains that have body-centered

orthorhombic and rhombohedral crystal symmetries, respectively. The corresponding orthorhombic and rhombohedral distortions of the fcc lattice introduce small but uniform strains within each tetrahedral grain.[35,36] Reinhard et. al[24] also noted that icosahedral structures in Ni, Ar, Cu, Au, Pb, and Ag have the general feature that the strain within each tetrahedron is non-uniform giving rise to a convex deformation of the outer facets.Since these structures are intrinsically strained, addition of pressure should alter the relative energetics of strain and surface energies which could have a large impact in the structural behavior of these particles.

The present study focuses on silver nanoparticles in the intermediate size range of 5–10 nm, which have been shown to possess an icosahedral structure in both free and substrate-supported cases. Silver supported on a substrate was investigated using scanning tunneling microscopy by Silly et al.[37] and was shown to adopt an icosahedral form. Similar structures were observed in unsupported silver clusters produced by an inert gas aggregation source and measured with electron diffraction.[24,40] Recent experimental measurements by Xing et al.[40] of small clusters of <100 atoms, showed size-dependent, fivefold symmetry which evolved to icosahedral symmetry with increasing size. Hall et al.[41] experimentally observed for larger clusters from 2–4 nm a mixture of icosahedral, decahedral, and fcc structures. More importantly, Reinhard et al.[24] showed a mixture of icosahedral and fcc structures for particles between 4 and 11 nm.

Bulk silver adopts the face-centered cubic structure. Under pressure, no phase transitions or distortions have yet been identified up to 200 GPa using shock compression methods [52] and up to 146 GPa using diamond-anvil cell (DAC) compression techniques[2].

More recently, 10 nm commercially available Ag nanoparticles were studied up to pressures of 30 GPa by Gu et al.[50] No phase transitions or noncubic distortions were observed in these experiments; however, a higher bulk modulus than that of bulk silver was noted.

Here we present experimental evidence that silver nanoparticles in the intermediate -size range of 5–10 nm in multiply twinned structures undergo a structural distortion consistent with a rhombohedral distortion with increasing pressure. Transmission electron micrographs of these particles show a mixture of morphologies including multiply twinned icosahedral structures. We propose a mechanism for this distortion based on the crystallographic structure and grain-boundaries of these particles. This hypothesis is consistent with a control experiment. We find that similar measurements on single-crystal fcc nanoparticles of platinum show no such distortion, which suggests that the grain boundaries are essential to the phenomenon.

3.3 Experimental

3.3.1 Nanoparticle synthesis and Characterization

Silver nanoparticles were synthesized via polyol reduction of silver perchlorate in refluxing toluene, with oleylamine and oleic acid as surfactants. Silver perchlorate (97%), 1,2-hexadecanediol (90%), oleylamine (70%), oleic acid (99%), ethylcyclohexane (99%), toluene, hexane, 2-propanol, pentane, and isopentane were purchased from Sigma-Aldrich (St. Louis, MO) and used as received. All solvents used were anhydrous and stored under inert atmosphere. All syntheses were performed under air-free conditions.

In a typical synthesis, 0.5 mmol 1,2-hexadecanediol was added to a round bottom

flask fitted with a condenser, thermocouple adapter, and a magnetic stir bar, and was evacuated and backfilled with argon. Oleylamine (0.6 mmol) mixed with 9.8 mL toluene was added to the reaction flask with vigorous stirring and brought to reflux at 110^{o}C. Once at reflux, 0.25 mmol $AgClO_4$ dissolved in 0.2 mL toluene was rapidly injected into the flask. Formation of nanoparticles occurred instantly upon mixing and was indicated by the originally colorless solution turning dark brown. After 2 min, 0.1 mL oleic acid was injected and the mixture was cooled to room temperature. The particles were cleaned under air-free conditions by precipitation with three volume equivalents of 2-propanol and centrifugation (4000 rpm for 5 min). Nanoparticles were resuspended in either toluene, hexane, or pressure-transmitting fluid (1:1 v/v pentane:isopentane or ethylcyclohexane). The average nanoparticle diameter was controlled by varying the time for particle ripening before the injection of the oleic acid up to a maximum of 24 h. Oleic acid binds to the particle surface more tightly than oleylamine does, thus it increases particle stability, and prevents growth at these temperatures.[67,68] Oleylamine likely serves dual purposes in this synthesis: (i) as an addition reducing agent and (ii) to act as a surfactant and control growth of nanocrystals in solution.[69]

Platinum nanoparticles of 2.8 ± 0.8 nm used in these experiments were synthesized by the polyol method of Sobal et al.[70] that is similar to the one outlined for Ag here. Transmission electron microscopy (TEM) measurements of these particles showed that they did not possess multiply twinned structures and were indeed single-crystal fcc nanoparticles.

The particle size was estimated by counting particles (n>3000) with TEM using a 200 kV Technai G^2 20. The samples used were synthesized from one month to one day in

advance of the high-pressure experiments and were stored cold in 1:1 pentane:isopentane, hexane, or toluene under an argon atmosphere in a refrigerator to prevent aggregation and degradation. The particle sizes were reaffirmed with TEM immediately before experimental x-ray diffraction (XRD) measurements.

Figure 3.1 shows a representative TEM image and histogram of nanoparticle diameter of a sample of silver nanoparticles used in this study. This particular sample had particles of diameter 7.2 $\pm$ 1.7 nm and is typical of the structure and size distribution of nanoparticles used in these experiments. The contrast variations in individual particles in this image are apparent indicating polycrystalline particles. There appears to be a mixture of particle morphologies showing that the particles are not spherical. This synthesis yields a mostly narrow size distribution.

Figure 3.2 shows a selection of high-resolution TEM images of the silver nanoparticles synthesized for these experiments. As predicted in the literature for the sizes of silver nanoparticles used in this study, the silver nanoparticles tended to be primarily multiply twinned particles approximating the idealized icosahedral structure.[24,43] Also observed are occasional single-crystal silver nanoparticles as shown in the center of this figure. Predominantly, though, we observed multiply twinned structures possessing twin pentajunctions.

All silver nanoparticle sizes and distributions presented in this study are shown in Table 3.1 . Particles shown with an asterisk were solvated in pressure-transmitting fluids that were not stored in inert atmosphere and were loaded in air.

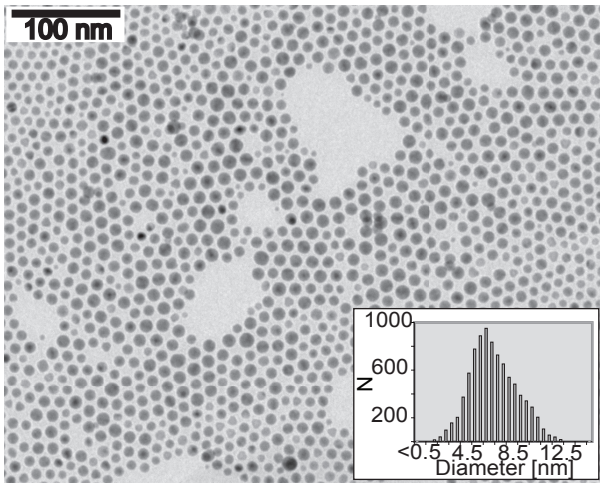

Figure 3.1: TEM of the 7.2 nm silver sample used in the x-ray diffraction. Histogram of nanoparticle size distribution is shown in the inset.

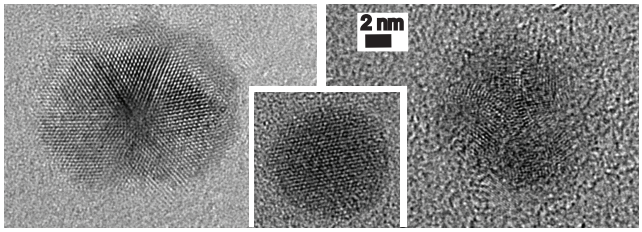

Figure 3.2: Representative high-resolution TEM images of silver nanoparticles used in the x-ray diffraction experiments. The samples used in this study primarily possessed multiply twinned domains (left and right images); however, single-crystal particles were occasionally observed (center image).

	Mean Diameter [nm]	σ**[nm]**
Ag	5.0	1.6
	2.6	1.2*
	7.2	1.7
	9.4	4.0*
	9.8	2.5
	10.0	3.0
Pt	2.8	0.8

Table 3.1: Table of silver and platinum nanoparticles' sizes and distributions used in this study. Asterisks indicate samples exposed to oxygen during sample loading.

3.3.2 High-pressure x-ray diffraction measurements

High pressure x-ray diffraction measurements were acquired on beamline 12.2.2 of the Advanced Light Source using an energy of 20 keV (λ=0.6199 Å).[71] The beam size was 50 x 50 μm. Patterns were acquired using a Mar-345 image plate. Typical acquisition times were between 15 and 20 min.

The sample was loaded in a DAC and centered relative to the x-ray beam vertically and horizontally on a rotation axis. The re-centering procedure was performed whenever the diamond cell was removed or remounted. Since the cell was removed to increase and to measure the pressure, this was repeated for every pressure step. In order to decrease signal from background air scattering, a small beamstop (second to one immediately before the detector) was placed behind the DAC.

The sample-to-detector distance and detector tilt were calibrated with a LaB_6 (NIST) standard. All two-dimensional (2D) XRD images were integrated to one-dimensional (1D) patterns using FIT2D [72], using a mask to exclude the two beamstops and single-crystal ruby diffraction spots from ruby loaded into the cell for pressure calibration (see later text).

A gas membrane-driven diamond-anvil cell (Diacell, Easylab, U.K.) with 400 μm diamond culets was used for high-pressure measurements. Spring-steel gaskets were preindented to 85 μm thickness and a centered 200-μm-diameter gasket hole was drilled with an electrical discharge machine (EDM). Several grains of annealed ruby were placed into the gasket hole to measure the pressure inside of the diamond cell.

Sample preparations were as specified throughout the text. Two preparations were used: one that allowed for the possibility of sample oxidation and the other intended to

prevent oxidation of the sample.

The sample was loaded in a 1:1 by volume pentane:isopentane mixture under an argon atmosphere in a glove box. A 1:1 V/V mixture of pentane:isopentane is hydrostatic up to 7 GPa, and it was used as the pressure-transmitting fluid because of its hydrostatic nature.[73,74] Additionally, silver nanoparticles not exposed to air are readily soluble in 1:1 pentane:isopentane unlike other pressure-transmitting fluids such as 4:1 methanol:ethanol. Alternatively, the sample was loaded in ethylcyclohexane under air. Ag nanoparticles exposed to air tended to precipitate from solution in 1:1 pentane:isopentane. The degree of hydrostaticity of ethylcyclohexane is unknown, but it has been the choice quasihydrostatic solvent of several high pressure experiments including those performed on nanoparticles.[10,11,75]

The sample was loaded to be sufficiently concentrated so as to give an adequate diffraction signal but still be visually transparent both in solution and in the diamond anvil cell. The solution color in the DAC was a light yellow to a light red color. If the solution of nanoparticles in the DAC was either opaque or a dark red color, or if visible aggregates formed, the cell was reloaded. Avoiding agglomeration is important to differentiate nanoscale effects from particle interaction effects at high pressures.

No gasket deformation was noticed during this study.

3.3.3 Pressure determination

The pressure in the diamond cell was determined using the pressure-dependent ruby fluorescence method.[76,77] Three to five pieces of annealed ruby grains in the cell were

used for measurements of the pressure. Values of the wavelengths (λ) of the R_1 and R_2 fluorescence emissions were obtained from the fit of two Lorentzian peaks to the fluorescence spectra. The pressure was determined by the relation $P = (\lambda - \lambda_{ambient})/0.365$ as in Ref. 76. The ambient values ($\lambda_{ambient}$)of R_1 and R_2 were measured by a single grain of annealed ruby placed on a microscope slide. The final pressure was determined by the average of the results for the R_1 and R_2 peaks. Spread in the pressure was calculated by the standard deviation of the results for all ruby peaks per each pressure measurement. The typical spread of pressures, below the pressure transmitting fluid glass transition, was on the order of <0.1 GPa. The degree of hydrostaticity was checked via the full width at half maximum of the fluorescence peaks and by the distribution of pressures across the cell. Throughout the experiment great care was taken to maintain the temperature of the DAC for both ruby and XRD measurements at 27-28^{o}C.

3.3.4 Data analysis

A background diffraction pattern was acquired after each pressure run with the diamond cell filled only with the pressure medium and a few grains of ruby. This pattern, in 1D format, was subtracted from each data set after it was scaled to match the integrated intensity and decay of the electron current in the storage ring. To determine the position and width, each peak in each XRD curve was fit with a Lorentzian peak using *Mathematica*.

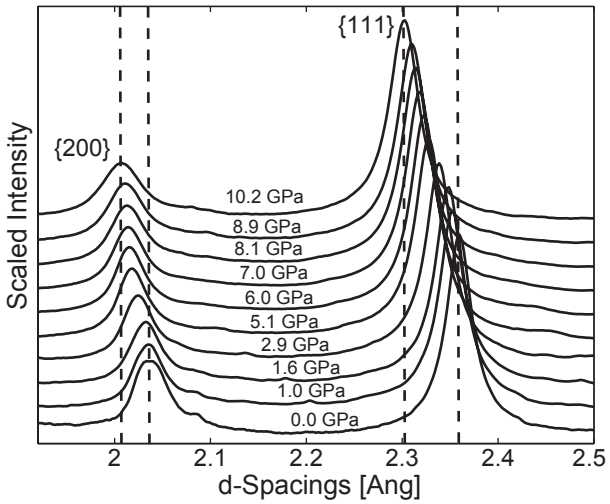

Figure 3.3: Stacked plot of the x-ray diffraction patterns of 9.4 nm silver nanoparticles compressed in a DAC from 0 to 10 GPa. The relative shifts of the {111} and the {200} peaks are not the same with pressure. Dashed lines are drawn as guides for the eyes.

3.4 Results

3.4.1 Silver nanoparticles

Selected x-ray diffraction data versus pressure for silver nanoparticles of 9.4±2.7 nm loaded in ethylcyclohexane are shown in Fig. 3.3. It is interesting to note that the relative shifts of the {111} and the {200} peaks are not the same with pressure.

Figure 3.4 shows the ratio of the d spacings of the {200} to the {111} diffraction positions of a 7.2±1.7 nm sample of silver nanoparticles. Since bulk silver metal adopts a fcc crystal structure up to a hydrostatic pressure of 150 GPa, each of the lattice directions in the cubic structure should compress isotropically. In a cubic crystal, the ratio of the {200} peaks to the {111} peaks should be $\sqrt{3/4} = 0.866$ and should stay constant with increasing pressure. We observe a distinct linear increase in the ratio of the d spacings with

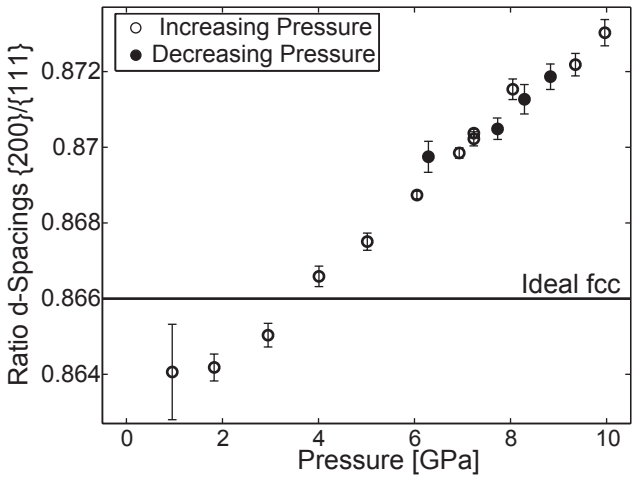

Figure 3.4: Plot of the ratio of the d spacings of the {200} peak to the {111} peak. This silver nanoparticle sample was 7.2 nm in diameter and was loaded in 1:1 pentane:isopentane under an argon atmosphere. Solid line corresponds to the ratio of an ideal fcc structure (0.866). This plot clearly demonstrates noncubic distortion with increasing pressure.

increasing pressure. Upon decompression, decreasing pressure points return along the same linear trend. In measurements where sample loss from the DAC with decreasing pressure is small, we observe full reversal of the distortion. This plot clearly demonstrates the noncubic behavior of silver nanoparticles as a function of pressure.

In Fig. 3.5, we show how the d spacings of the {111}, {200}, and {220} peaks for several sizes of silver nanoparticles change as a function of applied pressure. Figure 3.5A shows a histogram of the diameter of the different particles used in this experiment loaded in 1:1 V/V pentane:isopentane to fully demonstrate the size dependence of the noncubic distortion. In the plots, the * particles are those that have been exposed to oxygen post-synthesis. All other particles were prepared in an oxygen-free environment and loaded in the DAC in an argon atmosphere.

Figure 3.5B shows that for all sizes of Ag nanoparticles not exposed to oxygen,

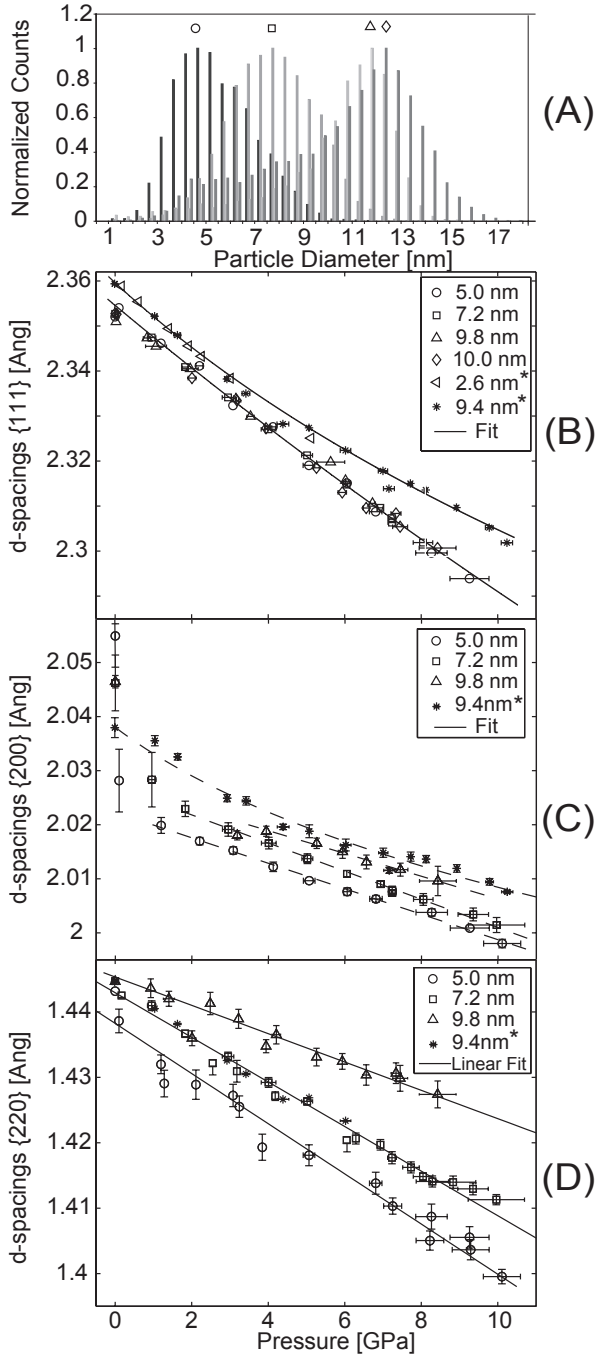

Figure 3.5: d spacings as a function of measured pressure. (A) Shows a histogram of nanoparticle sizes of the Ag samples not exposed to oxygen. (B), (C), and (D) are plots of the {111}, {200}, and {220} d spacings with pressure respectively. Lines are drawn on (B), (C), and (D) as guides for the eyes. Samples labeled with an * were exposed to oxygen during sample loading.

the compression of the {111} planes is, surprisingly, size independent. Particles exposed to oxygen show a similar trend also independent of particle size, but shifted to larger d spacings. Figures 3.5A and 3.5B show ,respectively, that the size dependence and distortion behavior are more apparent in the {220} and {200} planes. These plots show that there is size-dependent compression with increasing pressure that differs among the diffraction planes. Because of peak overlaps, the curve fits to obtain d_{200} were poorly behaved below 2 GPa so that these values may not be as accurate. The {220} peak demonstrates a linear pressure-dependent behavior that strongly depends on size. The amount of compression is less for larger particles along this direction.

As a guide for the eye, linear fits are made to the d spacings of the {220} reflection. For the {200} d spacings, a parabolic dashed line is drawn for the 9.4 nm particles and linear dashed trend lines are drawn for all other particles. For the {111}, with the small error bars and the small curvature, a similar trend line is drawn but generated with a fit of a Vinet equation.[78] The Vinet equation is a convenient and reasonable curve to fit this data. However, since these reflections do not behave as they would in the cubic materials, this fit has no physical meaning beyond a trend line. The Vinet equation is Eq 2.3. The values used to create the fit for the {111} d-spacings for silver nanoparticles loaded in oxygenated solvents are Ko = 100 GPa, Ko' = 10.0, do = 2.3596 and for those loaded in 1:1 pentane:isopentane are Ko = 110.6 GPa, Ko' = 2.4 and do = 2.3557.

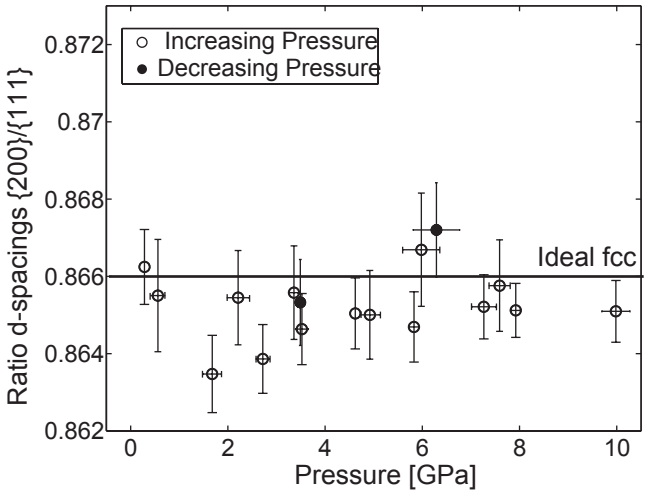

Figure 3.6: Ratio of the d spacings of the {200} to the {111} x-ray diffraction peaks in 3 nm platinum nanoparticles. A solid line is drawn at the d-spacing ratio for an ideal fcc structure. The plot demonstrates little deviation from cubic structure.

3.4.2 Platinum fcc nanoparticles

We performed control experiments with single-crystal fcc platinum nanoparticles in order to test whether the observed structural distortions in silver multiply twinned particles might (1) be an artifact of the measurement and/or data analysis methods or (2) appear in nontwinned particles, which would cast doubt on our results and proposed mechanism.

These particles were synthesized as described earlier; TEM measurements of these particles showed that they did not possess multiply twinned structures and were indeed single crystal fcc nanoparticles. Figure 3.6 presents the ratio of the $d_{\{200\}}/d_{\{111\}}$ from experimental x-ray diffraction peaks of platinum nanoparticles as a function of pressure. The data do not show the same noncubic distortion trend with pressure as was observed for Ag nanoparticles. The axes of this plot have been given the same scale as that of Fig. 3.4 to demonstrate the magnitude of this effect. Within the error of our measurements, platinum

retains its cubic crystal structure with pressure.

3.5 Discussion

Silver in the bulk adopts a fcc crystal structure at ambient conditions. Under increasing hydrostatic pressure, each of the lattice directions in the cubic structure should compress isotropically unless there is a driving nonhydrostaticity or a similar mechanism that causes the structure to deform anisotropically. This derives directly from the cubic symmetry; observation of something else indicates that something must be breaking that symmetry. Such a symmetry-breaking mechanism is the presence of twin pentajunctions that construct the ideally icosahedral morphology of intermediate-size silver nanoclusters.

For the two lower-symmetry structures (decahedra and icosahedra) that are the dominant idealized shapes of silver nanoparticles of this size range, two types of distortion are consistent: orthorhombic (decahedral particles) or rhombohedral (icosahedral particles).[35] In an orthorhombic distortion, the {111} peak from an undistorted fcc structure splits into two equal intensity peaks, the {200} separates into two peaks with one twice as intense as the other, and the {220} peak splits into three peaks with one four times as intense as the other two. This is accompanied by a concomitant shift of the d spacings.[35] In a rhombohedral distortion, a different scenario occurs with the {111} peak separating into two peaks with one a third the intensity of the other. The {200} peak remains unchanged, and the {220} peak splits into a doublet of equal intensity.[35] In our experiments, we more likely assign a rhombohedral distortion because (1) we see the {111} peak broaden possibly with the addition of a shoulder whereas it would be unchanged in an orthorhombic

distortion and (2) we observe no change in width to the {200} peak which would become a doublet in an orthorhombic distortion. This hypothesis is consistent with multiply twinned particles possessing icosahedral symmetry.

There are several scenarios that are potentially responsible for the noncubic distortion observed in Ag nanoparticles beyond that of the multiply twinned nature of the particles. These are: (i) a pressure-dependent deformation consistent with the elastic constants, (ii) the presence of an oxide layer on the particles, and (iii) nonhydrostatic conditions. Ruling out these possibilities is addressed here.

3.5.1 Elastic constants

We first consider that the stress may be nonhydrostatic and that an ensemble of randomly oriented particles may show an average deviation from cubic symmetry simply because some crystal directions are more compressible than others. If a bulk crystal deforms under a nonhydrostatic stress, the directionally dependent Young's moduli provide a good estimator of which direction the lattice will preferentially compress. The lattice directions with the smaller value of a directional Young's modulus will compress more.

The elastic constants, primarily the compliances, of bulk silver have been measured by several sources[79–84]–the most recent by Wolfenden et al.[84] Using the expressions for calculating the Young's modulus, E, outlined in Nye[85], Wolfenden's measurements can be presented in terms of directional Young's moduli as shown in Table 3.2.

This table illustrates that in bulk silver, the directionally-dependent Young's modulus, E, is greater in the <111> than in the <200> and <220> directions (E<111> >

Ag	E ⟨111⟩ [GPa]	E ⟨100⟩ [GPa]	E ⟨110⟩ [GPa]
	121.4	42.94	83.33

Table 3.2: Directionally dependent Young's moduli in GPa calculated from compliances of Ref. 84.

E<110> > E<100>). If the silver nanoparticles behaved like the bulk material, this would mean that the nanoparticles would more likely compress in the {200} direction than the {111} direction. For Ag nanoparticles we observe more compression along the {111} direction than the {200} direction, indicating that the observed distortion is unlikely to be caused by an interaction between nonhydrostaticity and elastic anisotropy.

3.5.2 Surface oxidation

Much of the effect of oxygen on the surface on nanoparticles is still not understood. It is known that thin silver films readily oxidize forming AgO and Ag_2O.[86] In some noble nanoparticle cases, indications are that it alters metal-metal bond lengths.[87] It is unclear what the effects of a surface oxide layer would be on these particular nanoparticles of silver. Detecting an appreciable surface oxide layer is also difficult since a monolayer or two of silver oxide will not possess a strong enough diffraction peak to render it visible in x-ray diffraction patterns or in electron diffraction.

In this study, to show that a surface oxide layer was not responsible for the observed distortion, we measured both particles that had been exposed to air and those loaded in inert conditions. Figure 3.3 presented a stacked plot of 9.4 nm Ag nanoparticles that had been loaded in air and in solvents not stored under inert conditions. A plot of the ratios of the d spacings for particles exposed to air also show noncubic behavior. As a comparison,

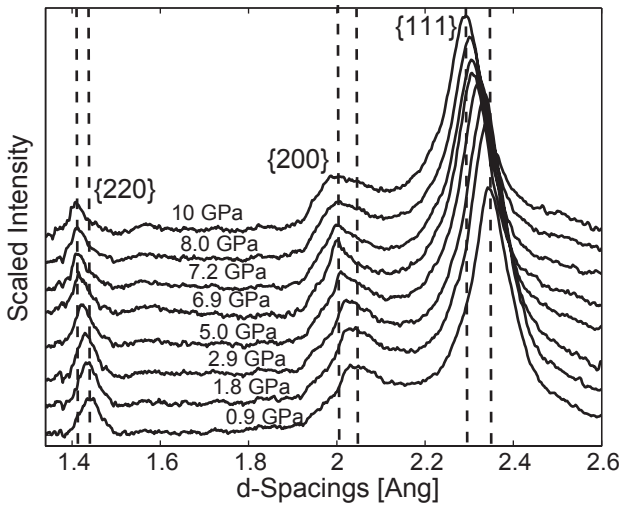

Figure 3.7: Stacked plot of the x-ray diffraction data of silver as a function of pressure clearly demonstrating noncubic behavior. This sample was 7.2 nm and was loaded in 1:1 V/V pentane:isopentane under inert atmosphere.

Fig. 3.7 shows a stacked plot of 7.2 ± 1.7 nm silver nanoparticles loaded under an inert atmosphere. A plot of the ratios of the d spacings for this data showing noncubic behavior is seen in Fig. 3.4. The strong {111} reflections compress more than the {200} and {220} d spacings.

In both samples exposed to air and those not exposed, a noncubic distortion of similar magnitude is observed. Therefore, the existence of an oxide layer is not entirely responsible for the noncubic distortion. However, as noted throughout the text, the oxide layer does indeed affect the behavior of the distortion in a quantifiable manner. It appears to have the effect of dampening the magnitude of the distortion and it gives rise to a relative shift of the d spacings from those particles not exposed to air during loading, preparation, and experimentation.

3.5.3 Nonhydrostatic conditions

To avoid nonhydrostatic conditions, it is necessary to have the nanoparticles fully solvated in the hydrostatic medium and dilute enough to prevent aggregation.

As an example of the effects of nonhydrostatic pressure on noble metal nanoparticles, recently, Guo et al.[88] presented results of agglomerated palladium nanocubes showing a distortion mediated by the packing strain of the nanocubes with increasing pressure in a nonhydrostatic pressure medium of silicone oil. They demonstrated that by unraveling the 2D XRD pattern of their nanoparticle into a plot of azimuthal angle vs. 2Θ, nonhydrostatic conditions resulted in a waviness of the x-ray diffraction pattern. This method is used in 2D quantitative texture analysis used to evaluate nonhydrostatic stresses.[89,90] We carried out a similar analysis on our x-ray diffraction patterns but did not find any waviness in the unraveled diffraction patterns indicative of nonhydrostatic compression. This is because our particles were well solvated in a hydrostatic medium and were not interacting.

In our experiments, as previously mentioned, we used ethylcyclohexane and a 1:1 by volume mixture of pentane:isopentane as pressure-transmitting fluid. The 1:1 pentane:isopentane mixture does not have a glass transition up to 7 GPa and is hydrostatic up to these pressures.[73,74] Ethylcyclohexane, based on the broadening of ruby fluorescence data acquired in this experiment, is likely only hydrostatic up to a maximum of 4 GPa. Despite the hydrostatic nature of these solvents and full solvation of our nanoparticles, we still observed the distortion behavior. Thereby we rule out nonhydrostaticity in our experiments as the driving cause of the distortion.

It is important to note that nanoparticles that are not agglomerated in the DAC,

as in our experiments, will be arranged in many different directions. Therefore, compression along one specific axis, as observed in our experiments, is unlikely. In addition, pressure gradients across the DAC are at most 0.4 GPa as determined from spatial variations of the ruby fluorescence. A pressure gradient of 0.4 GPa across the width of the gasket hole (0.3 mm in diameter) is sufficiently small such that a single nanoparticle (a few nanometers in diameter) will not experience any measurable local nonhydrostaticity.

3.5.4 Rhombohedral distortion

We recognize that the samples of Ag nanoparticles include a wide variety of particle morphologies, of which only a minority will closely approximate the idealized fcc, icosahedral, and decahedral forms. Each diffraction peak will therefore be a superposition of many peaks from the various lattice planes in these different morphologies. For concreteness and also to help clarify the mechanism that we propose in Sec. IVD, we analyze the d_{111}/d_{200} ratios as if all of the particles were icosahedral, and we further suppose that the curve fitting has identified the strong {111} peak in the icosahedral structure consistent with a rhombohedral crystal structure, which, as previously mentioned, has three times the intensity of the weak {111} peak. The following analysis is therefore not meant to be a precise accounting for the degree of crystalline distortion; rather, it is an estimate of the degree of distortion of a "typical" particle that would be required to explain the results. Thereby we consider these results consistent with grain boundary-mediated deformation due to the multiply twinned nature of the icosahedral structure of the silver nanoparticles in this intermediate-size range.

We calculate the amount of rhombohedral distortion from the ideal fcc crystal structure via the ratio of the d spacings of the {200} peak to the {111} peak. We represent the rhombohedral deformation as a matrix in reciprocal space, where a is the lattice constant and ϵ is a variable used to represent the amount of rhombohedral distortion as

$$\frac{2\pi}{a}\begin{vmatrix} 1 & 0 & 0 \\ 0 & 1 & 0 \\ 0 & 0 & 1 \end{vmatrix} \rightarrow \frac{2\pi}{a}\begin{vmatrix} 1 & \epsilon & \epsilon \\ \epsilon & 1 & \epsilon \\ \epsilon & \epsilon & 1 \end{vmatrix} \tag{3.1}$$

For the {200} direction, we calculate

$$\frac{2\pi}{a}\begin{bmatrix} 1 & \epsilon & \epsilon \\ \epsilon & 1 & \epsilon \\ \epsilon & \epsilon & 1 \end{bmatrix}\begin{bmatrix} 2 \\ 0 \\ 0 \end{bmatrix} = \frac{2\pi}{a}\begin{vmatrix} 2 \\ 2\epsilon \\ 2\epsilon \end{vmatrix} \tag{3.2}$$

Thus, the d spacings of the {200}, which is the inverse of the length of this vector, are

$$\frac{1}{d_{\{200\}}} = \frac{2\pi}{a}\sqrt{4+8\epsilon^2} \tag{3.3}$$

The {111} direction is more complicated to represent because there are eight total reflections: $\pm(111)$, $\pm(\bar{1}11)$, $\pm(1\bar{1}1)$, and $\pm(11\bar{1})$. We are primarily concerned with the position of the most intense reflection which gives the strong {111} reflection. In a rhombohedral distortion, the $\pm(111)$ reflection should be the weaker reflection.[35] We consider the d-spacing of the $(1\bar{1}1)$ reflection, whose d-spacing is equivalent to the remaining reflections,

$$(1\bar{1}1) \rightarrow \frac{2\pi}{a} \begin{bmatrix} 1 & \epsilon & \epsilon \\ \epsilon & 1 & \epsilon \\ \epsilon & \epsilon & 1 \end{bmatrix} \begin{bmatrix} 1 \\ -1 \\ 1 \end{bmatrix} = \frac{2\pi}{a} \begin{vmatrix} 1 \\ -1+2\epsilon \\ 1 \end{vmatrix} \tag{3.4}$$

with a corresponding d-spacing given by

$$\frac{1}{d_{\{111\}}} = \frac{2\pi}{a}\sqrt{3-4\epsilon+4\epsilon^2} \tag{3.5}$$

The ratio of the d spacings of the $\{200\}$ and the $\{111\}$ is

$$\frac{d_{\{200\}}}{d_{\{111\}}} = \frac{\sqrt{3-4\epsilon+4\epsilon^2}}{\sqrt{4+8\epsilon^2}} \tag{3.6}$$

Solving for ϵ gives the amount of distortion from the fcc structure. There are two solutions for ϵ from the solutions of the quadratic formula, but one of those is clearly unphysical since we ascribe ϵ (the amount of distortion) to be small. Figure 3.8 shows the amount of deviation from cubic symmetry, ϵ, assuming a rhombohedral distortion as a function of pressure.

At low pressures, it becomes increasingly difficult to fit the $\{200\}$ peaks to extract out the d spacings because at these low pressures, these peaks are broader and run into the tail ends of the $\{111\}$ peaks. At higher pressures, where d spacings can be fit from the $\{200\}$ peak more reliably, we see that each size of Ag nanoparticle follows a mostly linear trend in distortion versus pressure. At some pressure that varies with particle size, the amount of distortion returns to a zero value (basically cubic again) and then continues to rhombohedrally distort more in the opposite direction. Error bars are not shown for clarity

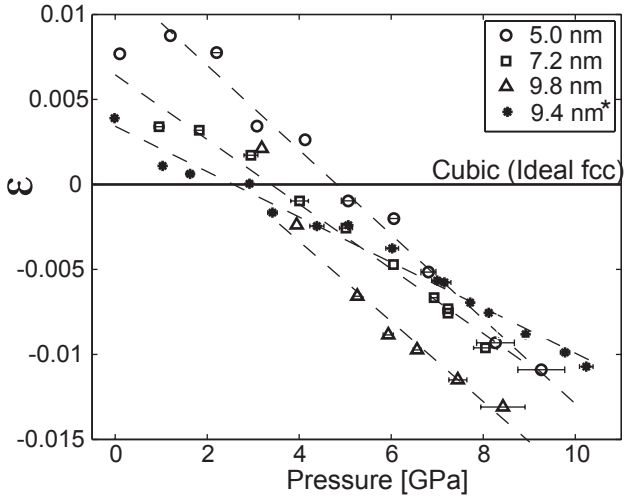

Figure 3.8: Degree of rhombohedral distortion, ϵ, as a function of pressure for a variety of nanoparticle samples as calculated in text. Sample labeled with an asterisk was exposed to oxygen during sample loading.

but are on the order of 0.0008 to 0.001 in ϵ. A line is drawn where $\epsilon = 0$; this is where the crystal structure resembles a more ideal fcc.

The slope of the rhombohedral distortion of the sample loaded in air is noticeably different while the others have similar slopes but different intercepts with lower epsilon-intercepts for larger particles. As we consider larger particle sizes, we presume that the amount of rhombohedral distortion needed to maintain an icosahedral structure should be less just because more of the atoms are far from the twin boundaries and thus more free to relax toward the bulk fcc form. Also this means that there should be less rhombohedral distortion with increasing pressure, and the return to a cubic non-distorted value should happen at lower pressures. As particle size decreases, there is more rhombohedral distortion, and a higher intersection pressure for a crystal structure resembling an ideal cubic structure.

This plot clearly demonstrates that: (i) the trends are statistically significant, (ii) the distortion is real, (iii) the distortion continuously varies with pressure, (iv) the distortion

and cubic intercept show size-dependent trends, and (v) the distortion is altered when a sample is exposed to oxidation.

3.5.5 Proposed mechanism

The data unambiguously show a departure from cubic symmetry in the ratios of the d spacings. TEM images suggest that the nanoparticles of this study share much of the essential crystallography (i.e., twin pentajunctions and exposed {111} surfaces) with the high-symmetry (icosahedral and decahedral), nearly-ideal structures reported by other groups, and thus it is expected that the particles should possess similar crystallographic distortions. For example, each tetrahedron in an icosahedron must, to maintain strain compatibility, compress in the {111} direction normal to its exposed face [Fig. 3.9A].[35] Keeping in mind that this morphology and detailed grain structure vary from one particle to the next, we can expect a statistical distribution of distortion parameters. The icosahedral and decahedral structures thus serve as idealized special cases phenomenologically similar to the particles actually being measured. Let us consider how our observed distortions may arise in such an idealized particle. Since we have found a distortion that is a very strong function of pressure that characteristically resembles a rhombohedral-like distortion, and even reverses in sign at a pressure that varies with nanoparticle size, we propose a mechanism for this transition based on the assumption of a rhombohedral-like distortion and on the bond distribution characteristic of the idealized case of a multiply twinned icosahedral particle.

There are 20 irregular tetrahedral pieces that constitute an ideal icosahedron.

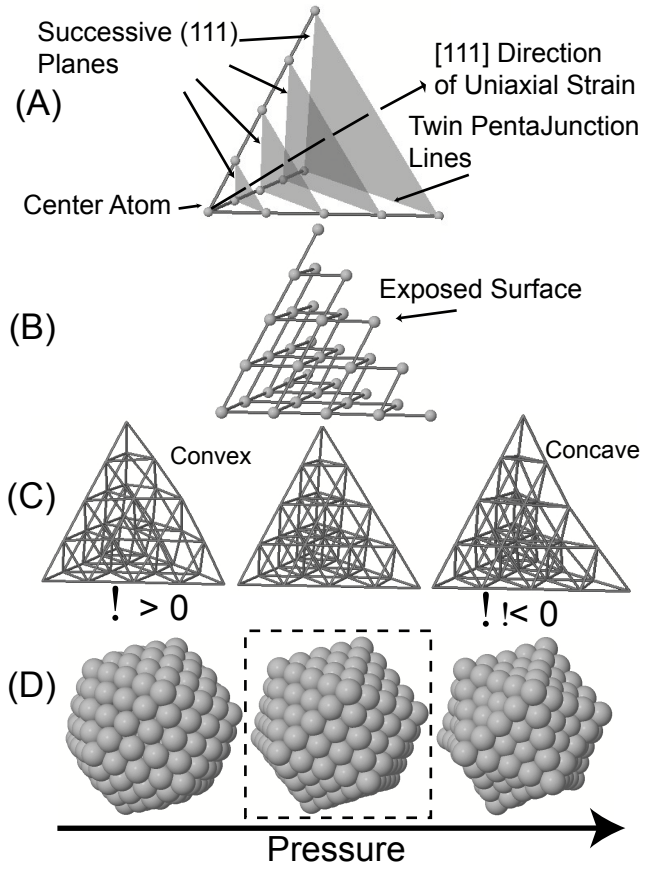

Figure 3.9: Illustrative diagram depicting (A) a schematic of a single distorted tetrahedron–1/20th of the icosahedron with only the (111) planes drawn. (B) The same tetrahedron in a ball and stick form, with only the short interplanar bonds drawn–the longer intraplanar bonds are removed for clarity. (C) The tetrahedron, now with all bonds shown, with a continuous distortion that would allow the effective average $d_{\{200\}}/d_{\{111\}}$ to vary. (D) The icosahedra resulting from the distortions in (C). A dashed box is drawn around the ideal undistorted icosahedron. ϵ is the degree of rhombohedral distortion described in text. Visualization of these structures was done with JMol Ref.. 92).

The crystallographic configuration possesses a rhombohedral structure that is the result of a uniaxial strain along a [111] direction in the fcc crystal to stabilize the atoms in the icosahedron.[35] Rhombohedral crystallography leads to a bimodal distribution of bond lengths. The packing of the atoms in this structure has been well described by Mackay.[91] To explain the proposed mechanism (detailed below), Fig. 3.9B presents an illustrative tetrahedron of these atomic arrangements and corresponding bonds. Here, only the shorter bonds have been drawn to illustrate the proposed mechanism of compression. In the icosahedral structure, for atoms that are in the {111} planes parallel to the exposed surface, the bonds between in-plane neighbors are longer, while the bonds between any two of these planes are shorter. Compressing normal to these planes is therefore more difficult than an in-plane compression as it would force the shorter bonds to become even shorter. It is far more likely that, as the pressure increases, the longer bonds will be subject to more compression than the shorter bonds.

The tetrahedron's other three {111} faces (the twin boundaries) consist of mostly shorter bonds, while most of the corresponding inter-planar bonds are longer. Therefore it should be easier to press these planes closer together than it would be for the planes parallel to the exposed surface. It is these three {111} directions that yield the strong {111} diffraction peak for the rhombohedrally distorted crystal, while the weak {111} peak corresponds to d spacings normal to the exposed face. Since we are assuming that the peak fitting in the data analysis is tracking the strong {111} peak, we would expect the {111} d spacings to show higher compressibility than would be expected for a cubic crystal. This is in fact exactly what we observe. However, symmetry and strain compatibility in the

icosahedral structure force the twin planes to remain essentially fixed throughout any such distortion, so that the anisotropic compression can only be accommodated by introducing an inhomogeneous strain within each grain. Recall Ref. 24, which shows that at zero pressure such a distortion produces a convex curvature of the exposed faces. We have found, by simulating such a distortion in a model [left column of Figs. 3.9(C) and 3.9(D); distortion exaggerated for clarity], that the resulting bond-length distribution corresponds to a positive value of our ϵ parameter. We then consider what must happen to this inhomogeneous strain as the pressure is increased, assuming (consistent with our measurements showing that the strong {111} peak is more compressible than expected) that the longer bonds will compress much more than the shorter bonds. This distortion corresponds to a gradual reduction, and eventually a reversal, in the curvature of the outer faces [middle and right columns of Fig. 3.9(C) and 3.9(D)] so that our measured ϵ parameter reverses in sign. We suggest, from the behavior of the x-ray diffraction patterns with decreasing pressure, that this presumed transition from convex to concave is elastic and reversible.

As alluded to earlier, with increasing nanoparticle size, more atomic layers are added to the icosahedral structure. Thus more of the atoms are in relatively bulk like regions far from the twin boundaries. The amount of uniaxial strain each atom takes up in the rhombohedral configuration becomes less; thus, the degree of rhombohedral distortion for bigger particles should be less thereby explaining the size-dependent trend observed in the data.

3.5.6 Lack of distortion in platinum fcc nanoparticles

It has been demonstrated that multiply twinned platinum nanoparticles transform into cuboctahedral-shaped single-crystal fcc nanoparticles with annealing and that platinum, unlike silver, often possesses fcc structure down to sizes as small as 10 Å.[93,94] Therefore, as a demonstration of a sample lacking a grain-boundary-mediated distortion that may become more evident with pressure, platinum serves as an ideal candidate and proves to be a useful control to rule out artifacts of the measurement.

Figure 3.6 presented the ratio of the Pt $d_{\{200\}}/d_{\{111\}}$ from experimental x-ray diffraction peaks as a function of pressure. The data do not show the same noncubic distortion trend with pressure as was observed for Ag nanoparticles. This provides evidence that the distortion behavior of Ag nanoparticles detected in these studies is the result of the multiply twinned pentagonal nature of the silver nanoparticles. This also serves as a useful test of our proposed mechanism based on the multiply twinned nature of the silver nanoparticles which is lacking in platinum nanoparticles.

3.6 Conclusions

This study clearly demonstrates that silver nanoparticles in the size range of 5–10 nm undergo a reversible noncubic distortion with pressure. The trends are statistically significant, the distortion is real, the distortion continuously varies with pressure, the distortion is size dependent, and the distortion is altered when a sample is exposed to oxidation.

We posed the question: what happens to the internal strain of multiply twinned structures if one introduces an external stress? In the case of silver nanoparticles, the

predominant ambient structure is multiply twinned and ideally icosahedral. The ambient strain is uniaxial along a [111] direction resulting in a rhombohedral distortion. The Ih silver nanoparticles have a convex appearance. Our results suggest that addition of pressure affects the nanoparticle such that the structure starts to bow more inward in a concave manner, becoming less convex, through a further rhombohedral distortion thereby altering the appearance of the icosahedron with pressure.

This study shows that cubic symmetry can be broken in fcc noble metal nanoparticles, e.g., through surface phenomena and twin pentajunctions, yielding rhombohedral distortions even at zero pressure that show pressure-dependent and size-dependent behaviors. The low energy per unit area of {111} surfaces and of coherent twin boundaries is able to compete with the energy per volume of the crystallographic distortion when dealing with small particles and grains under pressure.

Our results raise the question: is this an example of a really general phenomenon or would this happen in other materials with similar and different grain structures such as Dh gold or Ih palladium? Future measurements on other similar multiply twinned particles would help answer this question. Further calculations would also help elucidate the nature of this distortion in silver nanoparticles under pressure.

Chapter 4

Structural Distortion of 3.9 nm Silver Nanoparticles Under High Pressure

stereôn de gôniôn dôdeka, hupo pente epipedôn trigônôn isopleurôn periechomens hekasts, eikosi baseis echon isopleurous trigônous gegonen. kai to men heteron apllakto tôn stoicheiôn tauta gennsan, to de isoskeles trigônon egenna tn tou tetartou phusin, kata tettara sunistamenon, eis to kentron tas orthas gônias sunagon, hen isopleuron tetragônon apergasamenon: hex de toiauta

Plato Timaeus, 55b, on the Platonic solid: the icosahedron

4.1 Abstract

Silver nanoparticles in the size range of 5 – 10 nm have been shown to undergo a reversible linear pressure-dependent rhombohedral distortion. We have used x-ray diffraction from a synchrotron light source to investigate pressure-dependent trends in the crystal

structure of smaller, 3.9 nm silver nanoparticles in a hydrostatic medium compressed in a diamond-anvil cell. We demonstrate that 3.9 nm silver nanoparticles undergo a reversible structural transformation under hydrostatic pressures up to 8 GPa that is not consistent with the trend observed for intermediate sized nanoparticles. Results suggest a linear, orthorhombic distortion that continuously varies with hydrostatic pressures. We propose an interpretation of these results based on the idealized structure of decahedral silver nanoparticles rather than icosahedral nanoparticles and show a pressure-dependent orthorhombic distortion consistent with this interpretation.

4.2 Introduction

Silver nanoparticles exhibit optoelectronic properties, such as a surface plasmon resonance, that have wide-ranging applications in medicine, plasmonics and biosensing.[95–97] Silver nanoparticles are also useful for their antibacterial ad catalytic properties. Understanding how the thermodynamic structural behavior of silver nanoparticles scale is important in engineering nanoscale materials with specific properties for these applications. At small size scales, noble metal silver nanoparticles < 10 nm possess multiply-twinned polycrystalline structures possessing a fivefold symmetry that can be ideally interpreted as a decahedral (Dh) or icosahedral (Ih) structure. Adoption of these structures occurs because the reduction in surface energy more than offsets the energy cost of the internal strain and twin boundaries.[24] It is now widely recognized that slight differences in surface faceting and surface energy are sufficient to favor one atomic arrangement over another such as Dh vs. Ih.[41,42]

Silver nanoparticles from 1 to 4 nm have been shown to possess predominantly idealized decahedral structures.[24,43] In a decahedron, there are five identical tetrahedral twins around a five-fold axis. These subunits have {111} crystal faces which are arranged about the five-fold rotation axis parallel to the [110] direction. The internal strain associated with the fivefold symmetry of a multiply-twinned decahedral particle results in a distortion of the atomic arrangement from a face centered cubic lattice structure to a more body centered orthorhombic structure.

Several types of Dh structures have been identified as possible morphologies for silver nanoparticles in this size range. A regular decahedron is never observed, possibly because of the high energy required to have the corner edges with acute angles. One common shape is a round pentagonal particles in which the straight, sharp edges are replaced with smooth curves. An even more common shape is a truncated decahedron. This can either be described as a decahedron truncated along the sides or by a Marks decahedron which has extra {111} facets. The star decahedron is also often observed in very small particles[27]

In a previous study, the authors have presented evidence that silver nanoparticles in the size range of 5–10 nm undergo a reversible distortion under hydrostatic pressures up to 10 GPa that is consistent with a reversible linear pressure-dependent rhombohedral distortion. Silver nanoparticles in this size range were identified to possess structures predominantly described as icosahedra.[24,43]

Here we present an investigation of silver nanoparticles 3.9 nm which is in the size range where structures have been suggested to be predominantly describable as decahedra.

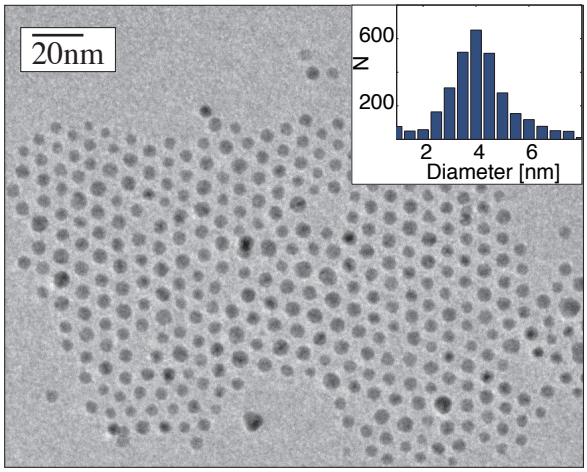

Figure 4.1: TEM image of 3.9 ± 1.4 nm silver nanoparticles taken immediately before x-ray diffraction experiments. Nanoparticle size distributions are shown in the inset.

4.3 Experimental

4.3.1 Nanoparticle synthesis and Characterization

Silver nanoparticles of the size, 3.9 ± 1.4 nm, were synthesized using the method presented in Chapter 3. The average nanoparticle diameter was controlled by limiting the time for particle ripening (∼ 5 min) before the injection of oleic acid. For more details on the synthetic method, the reader is referred to Chapter 3.

Figure 4.1 shows a representative TEM image and histogram of nanoparticle diameter of the 3.9 nm silver nanoparticles used in this study. The contrast variations in individual particles in this image are apparent indicating polycrystalline particles. The dark spots shown down the center of these particle are the likely events when the twin-pentajunction is lined up with the electron beam. There is a mixture of particle morphologies showing that the particles are not spherical structures and posses truncations and faceting. The particle size was estimated by counting particles (n>3000) with TEM using a 200 kV Tecnai G^2 20.

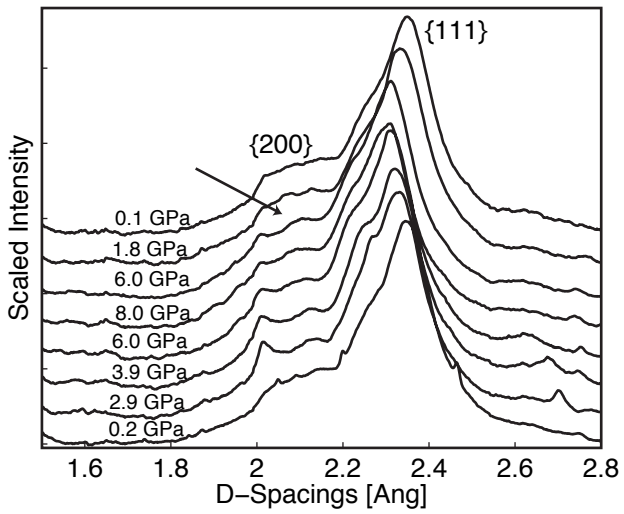

Figure 4.2: Stacked plot of 3.9 nm silver x-ray diffraction data. It is interesting to note that a peak is visible in the {200} peak at higher pressures.

The sample used was synthesized two weeks in advance of the high-pressure experiments and stored cold in 1:1 V/V pentane:isopentane under an argon atmosphere. The particle size was reaffirmed with TEM immediately before experimental x-ray diffraction (XRD) measurements. Figure 4.1 is a TEM image taken immediately before the x-ray diffraction experiments presented in this work.

High pressure x-ray diffraction measurements were acquired on beamline 12.2.2 of the Advanced Light Source using an energy of 20 keV (λ=0.6199 Å) and a beam size of 50 x 50 μm.[71] The 3.9 nm silver nanoparticles were loaded in a 1:1 V/V pentane:isopentane mixture under an argon atmosphere in a glovebox. This pressure medium was used because it has been shown to be hydrostatic up to 7 GPa[73,74] and it is an organic liquid mixture that the nanoparticles readily solvate into. The sample was loaded to be sufficiently concentrated so as to give an adequate diffraction signal but still be visually transparent both in solution and in the diamond anvil cell. The solution color in the DAC was a transparent light yellow

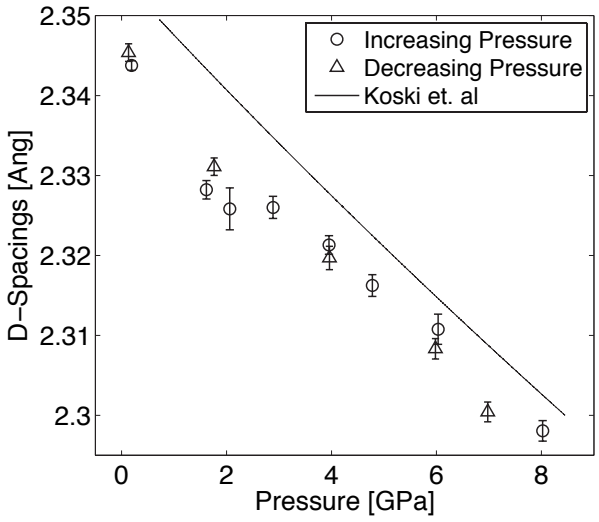

Figure 4.3: Plot of the {111} d-spacings of 3.9 nm silver data shown alongside the fits from Koski et al.[99].

color. Avoiding agglomeration is important to differentiate nanoscale effects from particle interaction effects at high pressures.

Further experimental details and the method of analysis are outlined in Chapter 3.

4.4 Results

Figure 4.2 shows selected x-ray diffraction data showing the {111} and {200} peaks for 3.9 nm silver nanoparticles compressed in a diamond anvil cell from 0 to 8 GPa. At such small size scales, due to Scherrer broadening,[98] it becomes very difficult to readily resolve these {200} peaks. We are able to resolve the {220} peaks (not shown). It is interesting to note that the {111} peak visibly broadens with pressure and also that a second peak is discernible at the location of the {200} d-spacing.

In Figure 4.3, the {111} d-spacings are plotted as a function of pressure along

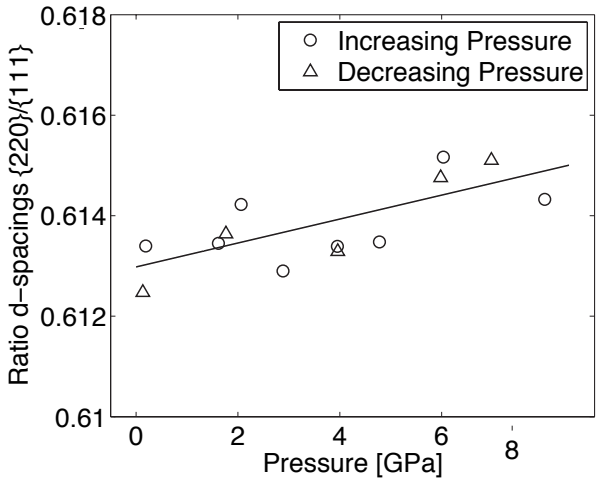

Figure 4.4: Ratio of the d-spacings of the {220}/{111} peaks for 3.9 nm silver nanoparticles.

with the fit of the d-spacings of the {111} peaks from Chapter 3. Previously for silver nanoparticles in the intermediate size range from 5-10 nm, it was shown that all the {111} d-spacings are the same regardless of size. This plot shows that below 5 nm, these 3.9 nm particles do not follow that same trend. Instead, the d-spacings are shifted to smaller values at this size scale. It is, however, important to note that this behavior is not seen in < 5 nm particles that have been exposed to oxygenated solvents as shown in Chapter 3 for 2.6 nm Ag nanoparticles.

By fitting the {220} peaks and the {111} peaks, we are able to extract the d-spacing values as a function of pressure and determine the ratio of the two. The ratio of the d-spacings of the {220} to {111} peaks is shown in Figure 4.4. As can be seen in this plot, the ratio of these d-spacings follows an increasing linear trend line. There is a large amount of scatter in the data due to the width of the peaks interfering with accurately determining the peak center.

4.5 Discussion

Two lower-symmetry structures (decahedra and icosahedra) have been proposed as the dominant idealized shape of silver nanoparticles from 1 to 10 nm. Two types of lattice distortion are consistent with these two structures: orthorhombic (which is actually body centered orthorhombic and characteristic of decahedral particles) or rhombohedral (icosahedral particles).[35] Silver in the size range of 1 to 5 nm has been shown to primarily posses decahedral character.[24,43] Using this assumed idealized structure, we interpret our patterns as distortion from fcc character to bco (body centered orthorhombic) character. In a body centered orthorhombic structure, the {111} peak from an undistorted fcc structure splits into two equal intensity peaks, the {200} separates into two peaks with one twice as intense as the other, and the {220} peak splits into three peaks with one four times as intense as the other two. This is accompanied by a concomitant shift of the d spacings.[35] We more likely attribute our x-ray diffraction patterns to bco because (1) we see a shift from the {111} d-spacings of our previous experiments, (2) we see a broadening of the {111} diffraction peaks, and (3) we see a shoulder in the {200} peak that we find consistent with simulated x-ray diffraction patters of 4 nm faceted decahedral silver particles.

4.5.1 Orthorhombic distortion

Samples of Ag nanoparticles will posses a variety of sizes and morphologies. The resulting x-ray diffraction pattern will be a superposition of the many diffraction peaks from the various lattice planes in these many particle morphologies. For clarity, we analyze the radio of the d-spacings, d_{220}/d_{111}, as though all of these particles are ideally decahedral.

$h_O k_O l_O$	$d-spacing$	fcc Correspondence
(011) (01$\bar{1}$)	$\frac{1}{\sqrt{0.527864+\frac{1}{(1+\gamma)^2}}}$	fcc {111}
(101) ($\bar{1}$01)	0.80902	
(110) (1$\bar{1}$0)	$\frac{1}{\sqrt{1+\frac{1}{(1+\gamma)^2}}}$	fcc {200}
(002)	0.68819	
(200)	0.5	fcc {220}
(11$\bar{2}$) ($\bar{1}$1$\bar{2}$) ($\bar{1}$12) (112)	$\frac{1}{\sqrt{3.11146+\frac{1}{(1+\gamma)^2}}}$	
(020)	$\frac{1+\gamma}{2}$	

Table 4.1: Table showing the correspondence between the fcc and orthorhombic hkl and the d-spacings in terms of the parameter γ described in the text.

We also assume that the {111} peak identified by curve fitting is the resulting doublet peak from the (011), (01$\bar{1}$), (101), and ($\bar{1}$10) in a body-centered orthorhombic structure and that the peak identified from the curve fitting of the {220} is the strongest reflection in those d-spacings corresponding to the (11$\bar{2}$), ($\bar{1}$1$\bar{2}$), ($\bar{1}$12), and (112).

Previously, we showed that the amount of rhombohedral distortion could be determined via the ratio of the d spacings of the {200} peak to the {111} peak. Using a similar method, we can relate the amount of distortion via the ratio of the d-spacings.

We calculate the amount of distortion, γ assuming that in the decahedral morphology, silver nanoparticles will posses a structure more akin to a body-centered orthorhombic structure. Without assuming that the planes that are closed-pack are the twins, we can represent the as a reciprocal space matrix similar to the analysis of a rhombohedral distortion

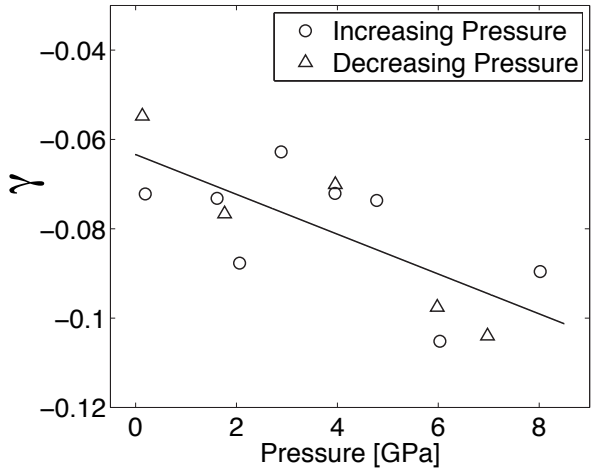

Figure 4.5: The amount of orthorhombic distortion, γ versus pressure. A linear trend line is drawn as a guide for the eye.

in Ref. 99.

$$\frac{2\pi}{a}\begin{vmatrix} 1 & 0 & 0 \\ 0 & 1 & 0 \\ 0 & 0 & 1 \end{vmatrix} \rightarrow \frac{2\pi}{a}\begin{vmatrix} 1 & 0 & 0 \\ 0 & \frac{1}{1+\gamma} & 0 \\ 0 & 0 & \frac{1}{Cot(36^o)} = 0.7265 \end{vmatrix} \tag{4.1}$$

Since we were only able to readily resolve the d-spacings of the {220} and the {111}, the ratio of those d spacings of the {220} and the {111} is:

$$\frac{d_{\{220\}}}{d_{\{111\}}} = \frac{0.80902 + \sqrt{0.527864 + \frac{1}{(1+\gamma)^2}}}{2\sqrt{3.1146 + \frac{1}{(1+\gamma)^2}}} \tag{4.2}$$

Yang et. al [35] presented an analysis of the x-ray diffraction parameters given the decahedral case assuming that the planes that are the exposed faces ({111} are closed-packed. This gives a solution of $\gamma = 0.05146$ for Yang et al. There is a second unique case, in which the twin planes are closed-packed but the exposed faces ({111}) are not and this gives a solution of $\gamma = -0.01775$. The parameter γ can be thought of as basically

how much the decahedron gets "squished" along its z-axis where z points out through the pentajunction of the decahedral.

We perform our analysis of the ratio of the d-spacings in a general case where we don't know γ. Table 4.1 presents the fcc and bco correspondence and what the d-spacing of the bco would be from this in terms of the parameter γ. To find the amount of orthorhombic distortion in the silver nanoparticle, given the ratio of any two d-spacings corresponding to the location of that fcc diffraction peak, is a matter of simply taking the ratios of the most intense reflection equation from this table and solving for γ.

Solutions to this equation yield four values for γ via solutions of the quadratic formula but since we ascribe the amount of distortion to be small, three of those values are clearly unphysical. The solutions for γ in this equation gives us the amount of orthorhombic distortion from the fcc structure as a function of pressure. Figure 4.5 shows the calculated γ from the ratio of thee $\{220\}$ and $\{111\}$ d-spacings as a function of pressure. It is interesting to note that γ is a larger negative value indicating that in these silver nanoparticles, assuming a decahedral morphology, neither the exposed faces ($\gamma = 0.05146$) nor the twin-faces ($\gamma = -0.01775$) are closed-packed.

In order to understand this, we simulated x-ray diffraction patterns of approximately 3.9 nm silver nanoparticles with $\gamma = -0.05146$, which is the negative of the situation where the exposed faces are closed-pack and a good approximation of our initial γ value, and with $\gamma = 0.0514$ as from Yang.[35] Figure 4.6 shows this simulated data. We simulated this pattern given the truncated decahedron in this figure which is a good approximation to a Marks decahedra[20] without the extra $\{111\}$ facets. This decahedral model, described

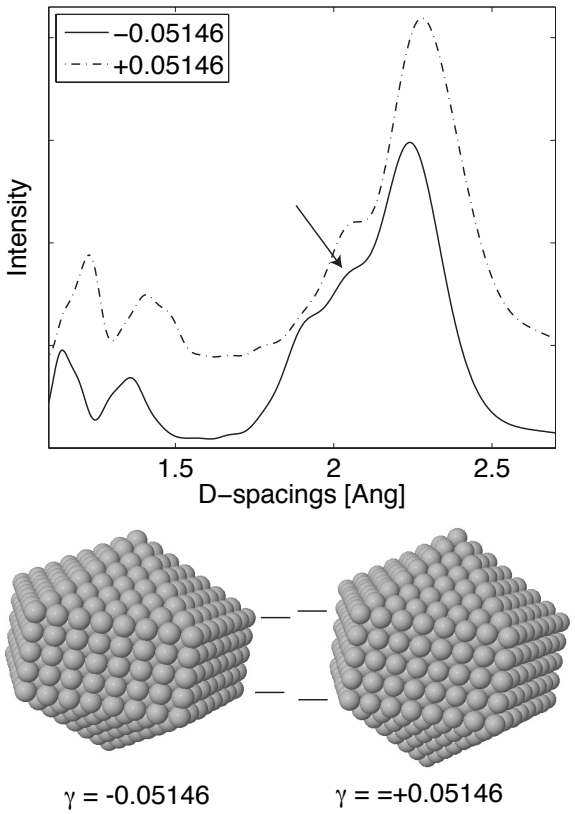

Figure 4.6: Simulated x-ray diffraction of 3.9 nm silver decahedral nanoparticles. The dashed line is a simulated XRD pattern given a positive γ value and the solid line is simulated given a negative γ value. The distortion of the decahedra is drawn below. γ expands or contracts the decahedra.

by Ino [21], is truncated by five (100) planes, parallel to the fivefold symmetry axis. One of the most notable features in this simulation is what appears to be an extra peak where the {200} fcc peak would be when γ is negative. Lines are drawn in this figure next to the decahedral structures to show how γ changes the size of the decahedra. It's thus reasonable to think of these silver nanoparticles as being idealized by a decahedron, probably faceted, with a negative gamma.

4.5.2 Proposed Distortion Mechanism

Previously we characterized and proposed a mechanism based on the bond length distribution assuming idealized icosahedral structures for 5 –10 nm silver nanoparticles and related bowing out of the {111} faces to those results.[99] The particular problem of the distortion of icosahedral structure is both non-linear and constrained.

At this smaller nanoparticle size scale of 3.9 nm, where silver nanoparticles are expected to be primarily idealized truncated decahedra, this problem becomes massively unconstrained. This is especially true in considering an idealized truncated decahedral structure in which the bco crystal has a nice linear way to distort because of the γ parameter that represents a simple uniform strain in the z-direction. tis degree of freedom may allow the structure to minimize the energy with a simple, linearly-varying distortion as pressure is applied, consistent with the data (Fig. 4.5).

In addition, there is a superposition effect to the x-ray diffraction pattern,specifically in this size range, where the XRD is weighted by the ensemble average of all the real different morphologies and sizes. Nor is it as easy to derive as much information as the larger

particles where the x-ray diffraction peaks were less broad but we still can develop what is going on in an average sense.

Basically we can say that this is still a way of quantifying the x-ray diffraction patterns in terms of a lattice structure, γ. We are unable to propose a mechanism similar to that proposed in Ref. 99. This also doesn't necessarily mean that the variation of γ is how the crystal is distorting because of the uniqueness problem wherein there are several solutions for possible distortion here but this is an appropriate way of quantifying this distortion from an fcc to orthorhombic structure.

4.6 Conclusions

This study demonstrates that 3.9 nm silver nanoparticles undergo a reversible noncubic distortion with pressure that is different from that of the noncubic distortion in Ref. 99. We find this trend is statistically significant and that this distortion continuously varies with pressure. We attribute this difference to the likelihood that, in the previous study, the nanoparticle sizes were such that the morphology could be described as ideally icosahedral and at this size the nanoparticle morphology can be described more appropriately as ideally decahedral.

Diffraction of these samples is complicated due to the ensemble average. It is recognized that silver nanoparticles in any given sample will not be all of one ideal morphology and that the contribution of a cluster to the scattering is proportional to their volume. Decahedra are always small in size so their relative contribution to the overall diffraction profiles will be very small in a sample with a wide range of particle sizes.

Although experimentally difficult due to the grain-size broadening effect in smaller particles, future studies on pressure-dependent distortion trends in smaller nanoparticles would be worthwhile. Further calculations would also help elucidate the pressure-dependent nature of this and other observed distortions in silver nanoparticles under pressure. Calvo and Doye performed a pressure dependent study of silver nanoparticles of varying morphology under pressure.[51] Further computational investigations would be invaluable.

Chapter 5

Detection of Pressure Gradients Across Hollow Nanospheres Using Encapsulated Silver Nanoparticles

Εικοσάεδρον συστήσασθαι χαὶ σφαίρα περιλαβεῖν· · ·

Euclid, Elements XIII.XVI, on putting an icosahedron in a sphere

5.1 Abstract

Evaluating the mechanical properties of nanomaterials is of the utmost importance for the future engineering of advanced materials. Hollow materials have long been recognized as both strong and lightweight. We experimentally demonstrate the measurement of pressure gradients across nanoshells of 3.4 nm thickness. Using a combination of in-situ high pressure x-ray diffraction techniques and sample recovery, encapsulating silver nanoparti-

cles in hollow metal oxide nanospheres provides a method to probe the thermodynamic environment inside a nanoshell. Thereby, with an encapsulated noble metal nanoparticle of silver, we are able to detect pressure gradients across hollow cobalt oxide and iron oxide nanoparticles and elucidate the mechanical properties of those shells. We show that these nanoshells have maximum resolved shear strengths on the order of 500 MPa to 1 GPa.

5.2 Introduction

Many sources have suggested nanomaterials as ideal materials for bulletproof jackets, revolutionary building materials, and other advanced engineered materials. Understanding the mechanical properties of nanoscale materials, then, is essential in predicting their response to mechanical stresses. Because of Hall-Petch scaling effect, which predicts that as a grain size gets smaller the yield strength of a material increases, nanocrystalline materials have attracted immense interest for their mechanical and technical applications. Nanocrystalline materials are usually strong but brittle. A great deal of research has gone into improving and investigating this. Having a method of probing the plasticity of one-grain-thick nanocrystalline materials could really open up the fundamental understanding of the mechanical properties of this whole class of materials.

At nanoscale sizes, it's difficult to measure the mechanical properties of single-grained thick nanomaterials. Either larger nanostructures (on the order of microns) or agglomerated grains of nanoscale materials can be studied.[100] Primarily, this is due to the experimental difficulty associated with having well-understood loading conditions, limitations in techniques to look at smaller materials, and because the shear strength depends on

the microstructure which is often polycrystalline thus complicating and impeding dislocation flow.[100]

For example, the most common technique to measure the mechanical property of a nanoparticle is indentation. This technique is limited by (i) the size of the nanoparticle relative to the indentation tip, (ii) the resolution limitation of AFM, TEM, or STEM in imaging the indentation, (iii) precise knowledge of the indenter geometry. Quantification of the loading conditions is very challenging especially in the cases of nonlinear and anisotropic material response.[101]

The primary difficulty in all these experiments is in quantifying the loading conditions. Also, it is difficult to measure indentations of very small nanoscale objects.

Several groups such as Xia [102] and Alivisatos [14,15] have demonstrated that it is possible to synthesize hollow nanospheres as well as to encapsulate various particles inside of these hollow nanospheres. We present a method wherein, essentially, by using a hollow nanosphere encapsulating a metal nanoparticle, we can measure the plasticity across one-grained thick materials using x-ray diffraction and traditional high pressure diamond anvil cell techniques. We measure the pressure inside the hollow nanosphere using x-ray diffraction of the encapsulated silver and the pressure outside using a traditional high pressure calibrant of ruby fluorescence. Hence we are able to detect pressure gradients across hollow cobalt oxide and iron oxide nanoparticles and elucidate the mechanical properties of those shells. In these experiments the loading is spherically symmetric unlike nano-indentation thus there are not as many assumptions that must be made about the loading conditions in order to determine the stress state in the material. Spherical symmetry also eliminates the

need for complex finite element analysis. Also, the typical thickness of a nanoshell measured in these experiments is on the order of 3 nm. Similar measurements on a 3 nm thin film would be difficult if not impossible using traditional techniques.

We show that these nanoshells have maximum resolved shear strengths on the order of 500 MPa to 1GPa. This allows us to evaluate the mechanical properties of hollow nanoshells.

In addition, high pressure x-ray diffraction can be used to measure the bulk moduli of the material, and though this cannot be related to the strength of nanoparticle, it gives another mechanical property of the nanoscale material.

Silver inside a nanoparticle is an ideal pressure probe of the external nanomaterial: it has a mostly cubic structure, its size-dependent deformation with pressure has been studied (see Chapters 3 and Ref. 99), it is relatively easy to synthesize inside a hollow nanosphere, silver is highly compressible thereby it is a sensitive pressure sensor (the bulk material has a bulk modulus of 100 GPa which is low for most transition metals), and it is a typical XRD high pressure calibrant so large amounts of bulk data are available.

5.3 Experimental

Silver nanoparticles were encapsulated by hollow nanoshells using a similar method to Yin et. al [14] and Shevchenko et al[105] for encapsulating platinum and gold nanoparticles in hollow nanospheres. For these studies, we encapsulated silver in both iron oxide and cobalt oxide hollow shells. Silver nanoparticles were synthesized using polyol reduction and coated with a cobalt or iron shell.[99,105] The shell was oxidized via the Kirkendall effect to

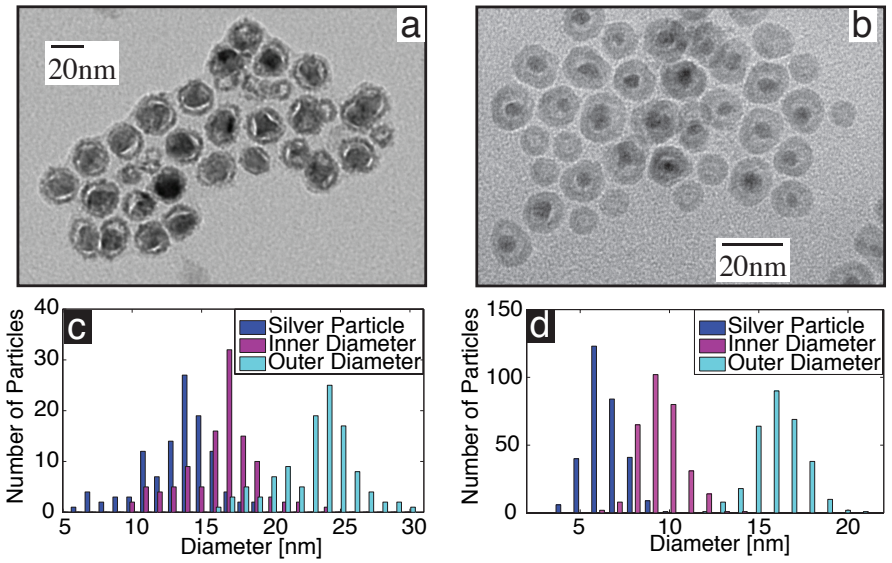

Figure 5.1: TEM image (b) and histogram of nanoparticle size distribution (a) of silver nanoparticles encapsulated in hollow iron oxide nanoshells used in these experiments. Representative TEM image (a) and histogram of nanoparticle size distribution (b)of silver nanoparticles encapsulated in hollow cobalt oxide nanoshells used in these experiments.

Table 5.1: Table of silver encapsulated hollow nanoparticle dimensions

	$Ag@Fe_3O_4$	Ag@CoO
Ag Particle [nm]	6.4 ± 1.0	12.9 ± 2.6
Inner Diameter [nm]	8.8 ± 1.26	15.9 ± 2.6
Outer Diameter [nm]	15.6 ± 1.7	22.7 ± 2.7
Shell Thickness[nm]	3.4 ± 1.0	3.4 ± 1.9

form hollow metal oxide shells.[14,105]

Transmission electron microscope (TEM) data were used to determine nanoparticle size and distribution. Nanoparticle grain size was confirmed with X-ray diffraction. Transmission Electron Microscopy images, Fig. 5.1(a) and Fig. 5.1(b), show that the nanoparticles are approximately spherical. Histograms of the size distributions of these particles are shown in Fig. 5.1(c) and Fig. 5.1(d) with means and standard deviations in Table 5.1.

The mechanical properties, structural stability, and shell pressure gradients in hol-

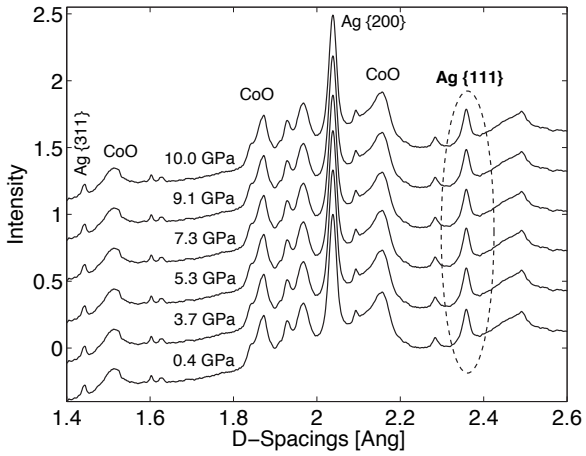

Figure 5.2: Representative Stacked Plot of

low metal oxide nanoshells were studied in a diamond anvil cell by high-pressure synchrotron X-ray diffraction[71] and ruby fluorescence techniques.[76,77] The nanoparticles were kept dilute in a solution of ethylcyclohexane and loaded in the diamond anvil cell. The particles were loaded to be sufficiently concentrated so as to give an adequate diffraction signal but still be, for the most part, visually transparent both in solution and in the diamond anvil cell. To differentiate nanoscale effects, and especially to prevent particles from mechanically interacting during measurement, avoiding agglomeration is essential.

The pressure outside the hollow nanospheres was measured using the pressure-dependent ruby fluorescence of ruby grains suspended in the diamond anvil cell in the hydrostatic pressure medium / nanoparticle fluid mixture of ethylcyclohexane.[76,77] The pressure inside the nanospheres and the lattice behavior of the shell material was measured via synchrotron X-ray diffraction. High pressure x-ray diffraction patterns were collected under hydrostatic (or quasi-hydrostatic at higher pressures) conditions.

5.4 Results

Representative X-ray diffraction patterns of silver encapsulated in cobalt oxide are shown in Figure 5.2. The cobalt oxide shell is a mixture of CoO and Co_3O_4 phases. Iron oxide shells used in these studies were identified to be all Fe_3O_4 phase. No phase transitions were observed in either material under pressure. Maximum pressure used in these experiments are 11 GPa below which neither of these materials has a phase transition.

Many notable results have been published that have shown that the properties of nanomaterials not only vary with composition but also with size and with structure. Thereby to fully evaluate the pressure using silver inside of a hollow nanosphere, we created a calibration curve. Several different sizes of silver nanoparticles were measured using X-ray diffraction, as a function of pressure, to generate this calibration curve presented in a previous work by the authors.[99] These experiments demonstrate that regardless of exact size, the {111} x-ray diffraction peak of silver nanoparticles in the intermediate size range of 5 to 10 nm has no size dependence. It is however dependent upon exposure to oxygen/oxygenated solvents.[99] Since the particles used for these experiments were exposed to oxygen, we choose to use the {111} x-ray diffraction peaks of those data as a calibration curve. As a convenient fit, we use the Vinet equation[78] to fit to the experimental data in this work, this pressure versus {111} d-spacings calibration curved thus allowed us to quantify the pressure inside a hollow nanosphere. The Vinet equation serves as a convenient fit this data; however it has no physical meaning. It is given in Eq 2.3; the values used to create the fit are Ko = 100 GPa, Ko' = 10.0, do = 2.3596.

We plot the measured values of the pressure inside the hollow nanospheres, as

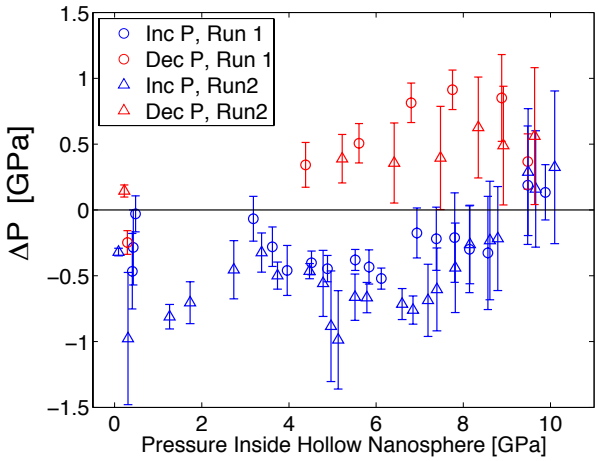

Figure 5.3: Pressure inside minus pressure outside the hollow nanosphere (ΔP) versus the external pressure as measured by ruby fluorescence of silver nanoparticles in ethylcyclohexane.

measured by x-ray diffraction minus the pressure outside the hollow nanospheres, as measured by ruby fluorescence, measured by x-ray diffraction (ΔP) versus the pressure inside as measured by the silver encapsulated cobalt oxide via X-ray diffraction in Figure 5.3. Data points for two separate runs under increasing pressure are shown in blue while data points under decreasing pressure are shown in red. The error bars in Fig. 5.3 are dominated by the precision of the ruby measurement.

5.5 Discussion

One of the unique properties inherent in the compression manner of this experiment is that it's spherically symmetric. This means that the elastics problem is relatively easy to solve and there is no need for advanced finite element code to understand the results. Hence analytic and numerical solutions can easily be determined and evaluated from the

measured mechanical properties of these materials.

5.5.1 Yield Strength

Assuming the material has plastically yielded (which should happen quickly for the pressure values of loading used in these experiments), the difference of pressure, ΔP from the inside, radius = a, to the outside, radius = b, of a hollow nanosphere can be related to the maximum resolved shear strength of the shell material (the yield strength), Y, by:

$$|Pa - Pb| = Y\sqrt{2}\left(1 - \frac{a^3}{b^3}\right) \tag{5.1}$$

My derivation of this equation is covered in Appendix A. The pressure difference, across a shell, from the inside to the outside is a function of two primary parameters. The first is the yield strength of the material and the second is a geometric factor which is the ratio of the cubes of the inner and outer radii.

Although we don't know the exact geometry (inner, a, and outer radii, b) of the nanospheres under increasing pressure, we extract a reliable number for the yield strength by assuming that the relative sphere dimensions do not change much during deformation. For the purposes of these results, we calculate pressure gradients as an average of pressures below about 6 GPa to avoid the regions where the dimensions of the hollow sphere may be altered most.

In addition to pressure gradients across our hollow nanospheres, we were able to extract out the bulk modulus of the shell material. Table 5.2 presents the measured bulk

Table 5.2: Table of experimentally determined mechanical properties

Nanoshell	Bulk Modulus [GPa]	Literature Bulk Modulus	ΔP	Y [Gpa]
Ag@Fe_3O_4	148 $\pm$ 5	186	$\sim$ -0.74 GPa	0.64
Ag@CoO	191 $\pm$ 10	190.5	-0.48 GPa	0.52

modulus, the average pressure difference across the shell averaged from values less than 6 GPa, and the yield strength calculated from equation 5.1. Yield strengths are typically on the order of less than a few hundred MPa.

5.5.2 Sample Recovery

Since the pressure inside the sphere returned approximately to it's initial value upon decompression, we performed sample recovery experiments to determine if the sphere size or shape was altered with pressure or if there was irreversible or reversible buckling of the hollow nanospheres.

Samples recovered after pressurization show that the hollow nanospheres have remained intact. As an example, Figure 5.4 shows TEM images of samples recovered after pressurization to 10 GPa. Samples recovered are Ag encapsulated in cobalt oxide (Fig. 5.4a) and iron oxide (Fig. 5.4b). These images show that the hollow spheres are still intact in both materials indicating that no irreversible buckling occurred up to 10 GPa. Analysis of the recovered nanoparticle dimensions shows no alteration after pressurization to within counting error bars demonstrating full recovery.

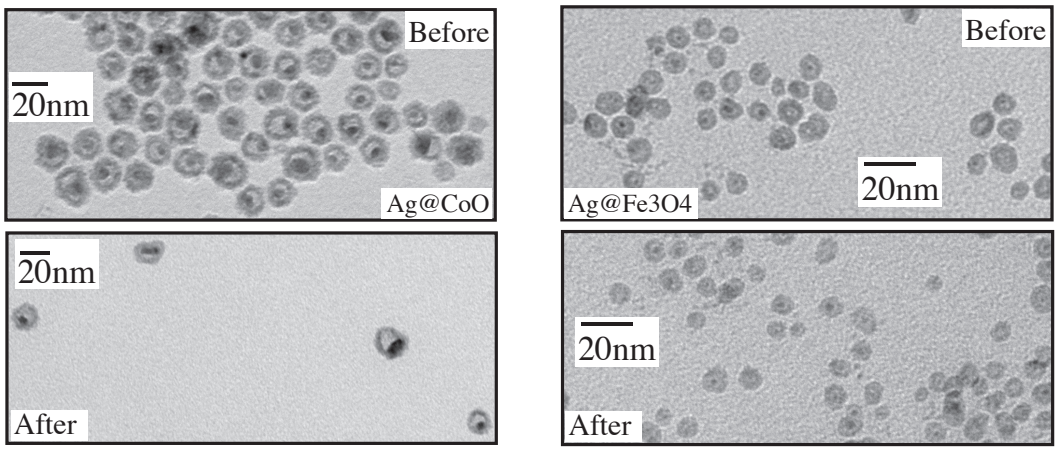

Figure 5.4: Silver Nanoparticles encapsulated in (a) cobalt oxide and (b) iron oxide before and after pressurization.

5.6 Conclusions

Hollow nanoparticles of varying material can be generated using the nanoscale kirkendall effect. We present a way of measuring the mechanical properties of a nanoscale material only a grain thick. It was determined that the yield strength across a hollow nanosphere is on the order of 500 MPa - 1 GPa. Typical values for steel are on the order of 400-800 MPa. Hence, these metal oxide hollow nanoparticles are very strong. These measurements could not have been made with present indenter techniques due to the small size of the nanoparticle and resolution limitations of present indenter techniques. Using x-ray diffraction of encapsulated Ag metal nanoparticles and diamond anvil cell methods to experimentally determine the mechanical properties of a hollow nanosphere and assuming spherical symmetry is a viable way to determine these properties that avoids using finite element codes.

Further work that would be interesting to pursue is to correlate the spread of

pressure gradients from the peak widths and also to explain whether the crossover at 9GPa is due to buckling or not. It would also be interesting to determine the involvement of the hydrostatic pressure fluid, ethylcyclohexane, and glass transitions thereof, in these measurements.

Chapter 6

High Pressure X-ray Diffraction on Multi-branched Platinum Tetrapods Encapsulated in a Cobalt Sulfide Nanoshell

I tell you, we haven't begun to discover what science can do to the body and mind of man!
Henry Jekyll MD (Dr. Jekyll and Mr. Hyde 1920)

6.1 Introduction

There is significant technological interest in the wiring up of nanorods and nano-sized tetrapods for electronic applications.[108–110] These structures show unique electronic and conduction properties. These types of branched and elongated structures can also

be synthesized from semiconductor materials and noble metals.[104] It has also been shown that a metal nanoparticle can be encapsulated by a metal particle by a hollow metal oxide nanosphere.[14,105] The combination of these methodologies (encapsulation and nanoparticle branching) may have future relevance for other electronic applications. Analyzing the pressure dependence of such structures may provide unique insight into future engineering of such materials.

Previously, in Chapter 5, we showed that x-ray diffraction measurements coupled with diamond anvil cell techniques of silver encapsulated by a metal oxide could be used to measure the pressure gradients across a hollow nanosphere. In this chapter, I present a unique case where non-spherical nanoparticles were encapsulated in hollow nanospheres. Multi-branched platinum nanoparticles were encapsulated in hollow cobalt sulfide shells. Using a similar technique as Chapter 5, we experimentally determined the pressure inside the hollow sphere using x-ray diffraction from a synchrotron source and high pressure diamond anvil cell techniques. The question posed in this research is "How does the structural nature of a particle and the lack of a controlled stress state affect the behavior of a metal nanoparticle in a hollow sphere."

6.2 Experimental

6.2.1 Nanoparticle synthesis and Characterization

Tetrapods of platinum are easily synthesized via a polyol reduction.[103,104] For our purposes, we wanted a branched platinum tetrapod like structure that was small enough to fit into the hollow nanospheres.

Platinum nanoparticles were encapsulated by hollow nanoshells using a similar method to Yin et. al [14] for encapsulating platinum nanoparticles in hollow cobalt sulfide nanospheres. For these studies, we encapsulated multi-branched platinum nanoparticles in a cobalt sulfide shell via coating with cobalt and sulfidation via the Kirkendall effect.[14,16]

Multi-branched platinum nanoparticles were synthesized via the polyol process of Sobal et al [70] where to form the branched shape, an excess of oleylamine (double the amount for a spherical platinum nanosphere synthesis) is added. More amine means faster nucleation, which means large particles and this leads to a loss of spherical shape.

Initially, 300 mg of 1,2-hexadecanediol (90% tech grade from Aldrich) and oleylamine (0.2 ml, 70% tech grade from Aldrich) is degassed under an argon atmosphere. Triocytylphonsphine (0.06 mL) and oleic acid (0.2 mL 99% from Aldrich) in 15 ml of 1,2-dichlorobenzene (99.8% anhydrous, Aldrich) is injected into the flask. The solution is brought to reflux at 1860^{o}C. Once under reflux, 150 mg of platinum acetylacetonate (97%, Aldrich) solvated in 5 ml of 1,2-dichlorobenzene is rapidly injected into the refluxing solution. Formation of nanoparticles occurs quickly upon reaction and is indicated by the yellow solution turning black. The solution is kept at reflux for 2 hours.

The cobalt sulfide (Co_3S_4) shell is grown around the platinum multi-branched particles by slowly injecting 1.08 g of $Co_2(CO)_8$ solvated in 6 mL 1,2-dichlorobenzene. The solution was refluxed for four minutes. Then, 0.258 g of sulfur in 10 mL of 1,2-dichlorobenzene was added. The solution was refluxed an additional three minutes. The nanoparticles are cleaned with two volume equivalents of ethanol and re-dissolved in ethylcyclohexane (99+% from Aldrich), hydrostatic pressure medium.

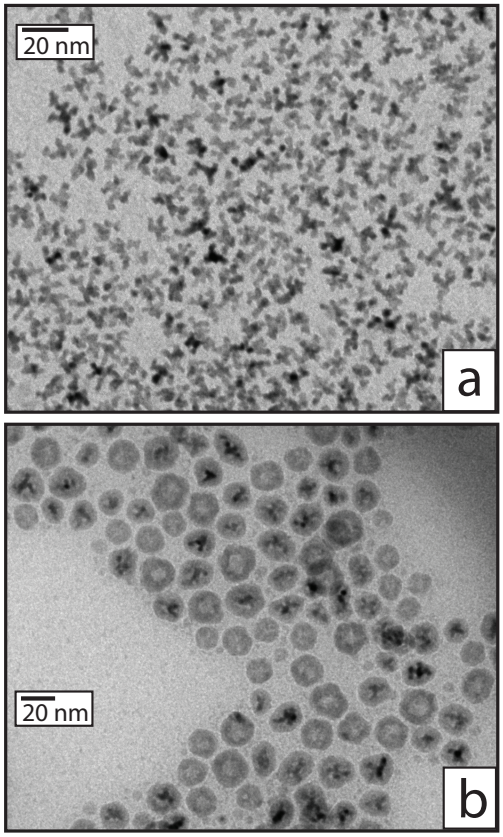

Figure 6.1: TEM of platinum branched particles before and after encapsulation with cobalt sulfide.

Transmission electron microscope (TEM) data were used to determine nanoparticle size and shape. Nanoparticle grain size was confirmed with X-ray diffraction. Transmission Electron Microscopy images, Fig. 6.1(a) and Fig. 6.1(b), show the platinum nanoparticles before and after encapsulation with cobalt sulfide respectively.

The multi-branched platinum nanoparticles have a tetrapod-like shape. Platinum spheres have a cuboctahedral structure.[27] A cuboctahedral structure has {111} and {100} planes exposed to the surface (see Fig. 2.1). It is assumed that growth of these shapes is in the four different {111} directions with the surfaces being {110} planes is the obvious guess as the low energy surface. After encapsulation, the branched platinum particles are seen to touch the shell wall at each of the branch ends and are kept in a confined stress state by the nanoshells.

6.2.2 High Pressure x-ray diffraction experiments

All high pressure experiments were performed in a diamond anvil cell by high-pressure synchrotron X-ray diffraction[71] and ruby fluorescence techniques.[76,77] The pressure outside the hollow nanospheres was measured using the pressure-dependent ruby fluorescence of ruby grains suspended in the diamond anvil cell in the hydrostatic pressure medium / nanoparticle fluid mixture of ethylcyclohexane (see methods).[76,77] The pressure inside the nanospheres and the lattice behavior of the shell material was measured via synchrotron X-ray diffraction. High pressure x-ray diffraction patterns were collected under hydrostatic (or quasi-hydrostatic at higher pressures) conditions.

The nanoparticles were kept dilute in a solution of ethylcyclohexane to avoid ag-

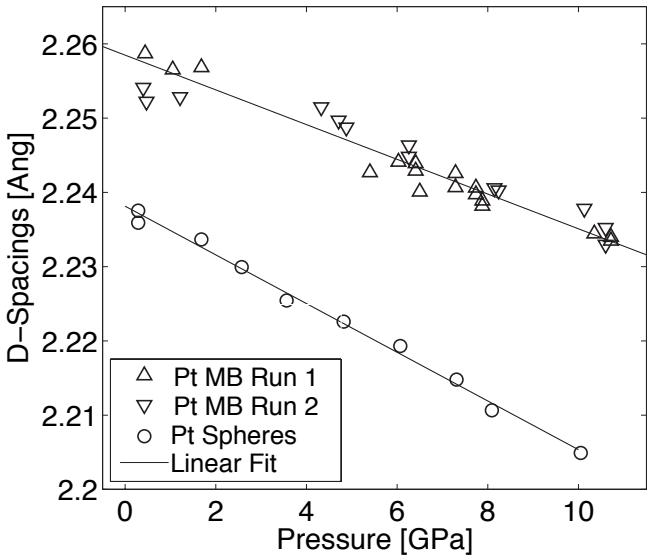

Figure 6.2: Calibration curve of the readily resolved {111} x-ray diffraction peaks acquired from the un-encapsulated platinum branched particles. The d-spacings of 2.8 nm platinum spherical nanoparticles are plotted on the same axis to show how greatly the d-spacings are altered for these larger particles.

glomeration effects and loaded in the diamond anvil cell. The particles were loaded to be sufficiently concentrated so as to give an adequate diffraction signal but still be, for the most part, visually transparent both in solution and in the diamond anvil cell. To differentiate nanoscale effects, and especially to prevent particles from mechanically interacting during measurement, avoiding agglomeration is essential.

Further details of these experimental techniques can be found in Chapter 3 and Chapter 5

6.3 Results

Figure 6.2 shows the calibration curve of the {111} d-spacings vs. pressure. Bare platinum branched particles (with no cobalt sulfide) were measured as a function of pressure

to act as a calibrant of the d-spacings vs. pressure. A large scatter is seen in this data, despite sharp x-ray diffraction peaks, perhaps due to the crystallographic nature and strain state of the platinum particles. The results were interpreted similar to Chapter 4 and Chapter 3 wherein silver nanoparticles were used a pressure calibrant. In this plot, the d-spacings of 2.8 $\pm$ 0.8 nm platinum nanospheres are included for comparison showing the different behavior of these two very different types of nanoparticles (as compared to Chapter 5). A linear fit is drawn as a guide for the eye. The slopes of both fits change dramatically with the crystallographic structure of the platinum nanoparticle.

A benefit of these multi-branched particles is that they don't change shape or size with addition of the cobalt layer and later sulfidation unlike spherical nanoparticles which do change size due to the extra amount of time under reflux. Attempts at using spherical platinum as a probes of the pressure inside proved difficult due to the low compressible nature of platinum as well as the difficulty in achieving a reliable size sphere in the hollow sphere.

In Figure 6.3, the resulting pressure inside vs. pressure outside is plotted. It is interesting to note that all pressures measured inside the sphere are greater than the pressure outside the sphere for two different runs/loadings. The same behavior is observed in both runs and is thus repeatable.

6.4 Discussion

The peculiar crystallography of these multi-branched platinum nanoparticles makes this a very different case from Chapter 5. The structure of the platinum nanoparticle en-

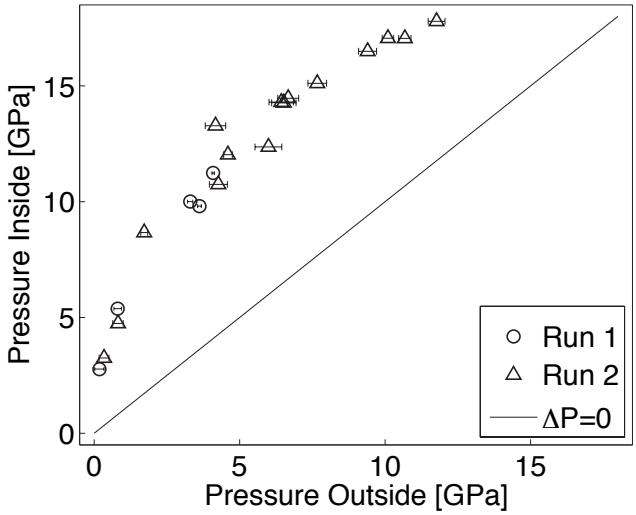

Figure 6.3: The pressure inside the hollow sphere as calibrated by Fig. 6.2 vs the pressure outside the hollow sphere as measured by ruby fluorescence. Note the greater pressure inside the hollow nanosphere.

capsulated in a hollow nanosphere alters the pressure response from expected and from that previously observed for spheres encapsulated in hollow spheres. Here, the multi-branched particles are touching the surface at more than one point and thus may be in a unique stress state.

A second difference between the case of the silver encapsulation and this are that a cobalt oxide shell was used in the silver case (to prevent any sulfur interaction with the silver) whereas the platinum case presented here used a sulfide shell. A priori that shouldn't make a huge difference in the pressure response. There will be a different interface energy between the sulfide versus the oxide material but that will not be a huge effect.

These are interesting results in which the stress state is not fully interpretable. The multi-branched platinum case is unique in that it is not a de Wulf minimized structure. In other words, this is not an equilibrium structure. What is observed is that the pressure

is much higher in the spheres for these branched platinum particles due most likely to the confined nature and uncontrolled stress state. A full interpretation of these results require more complex finite element calculations.

6.5 Conclusions

Nanocrystals are often externally faceted showing a defined shape which is directly related to their crystallographic structure. In this case, the platinum structure is controlled by the kinetics of how it grew of which we assume that growth is in the four different {111} directions. The surfaces being {110} planes is the obvious guess as the low energy surface. The crystallography of nanostructures can have unique effects with pressure. Encapsulation of such structures with a hollow nanosphere yields interesting, though not readily interpretable, results.

What these results show is that the experiment with the multi-branched platinum nanoparticles produces results that, analyzed the same way as the results of Chapter 5, are not easily understood. There is no way the strength of these materials is so high as to support such a huge gradient. I think what can be gained from these results is speculative in that there is a lack of a controlled stress state when the nanoparticle is flexible and touches the shell at several widely-spaced points.

Chapter 7

Supplementary Experimental Information

7.1 High Pressure: Diamond Anvil Cell

All high pressures presented herein were generated using a diamond anvil cell (DAC). A schematic of a basic DAC is shown in Figure 7.1. All x-ray diffraction experiments presented here used either gas-membrne, piston-cylinder type DACs or Merrill-Bassett type DACs. Gas membrane-driven DACs (WCME-DAC, now Easylab, United Kingdom) from Diacell were used for precise control of the applied load and for the ability to increase pressure remotely. These types of cells apply load by means of gas pressure inflating a bellows in contact with the piston Diamond anvils are mounted on a tungsten carbide and beryllium backing plate respectively. The Be backing plate is kept downstream of the x-ray beam to allow maximum transmission of the x-ray beam (5 mm of Be absorbs

approximately 20% of incident 20 keV photons). A metallic gasket of spring steel is used both to maintain hydrostatic pressures and to keep the nanoparticle dissolved in pressure transmitting fluid sample in the cell. Type 1A diamonds of 1/4 carat weight with either an 8-sided or 16-sided brilliant cut were used for these experiments. Gaskets were prepared by first indenting the metal using the DAC to a predetermined number of turns and then drilling 150-300 micron diameter holes in the indented metal. Gasket thickness ranged from 60-100 microns depending upon the experiment. Gasket holes were drilled with an electronic drilling machine. A review of diamond anvil cell techniques can be found in Ref. 111 and Ref. 1

7.2 Ruby Fluorescence

Pressures were determined by the ruby fluorescence technique of three to five annealed grains of ruby placed in the diamond anvil cell.[76,77] Fluorescence was excited with an argon ion laser at wavelength of $\lambda = 488nm$. Ruby fluorescence was collected with an in-house system designed by Sander Caldwell at Beamline 12.2.2 of the advanced light source. Spectra were collected with a Princeton Instruments Pixis CCD camera and an Acton spectrometer. Collection times ranged from 1-60 seconds. Accumulations times of one second for Ag nanoparticles were common yet accumulations times upwards of 60 seconds were required for the metal oxides presented here because they strongly absorb the fluorescent ruby signal. The system resolution was about ± 0.02 nm (approximately 0.05 GPa). Two Lorentzian peaks were fit to the fluorescence emission to obtain values of the wavelengths of the ruby peaks, R_1 and R_2. The pressure was determined by the relation

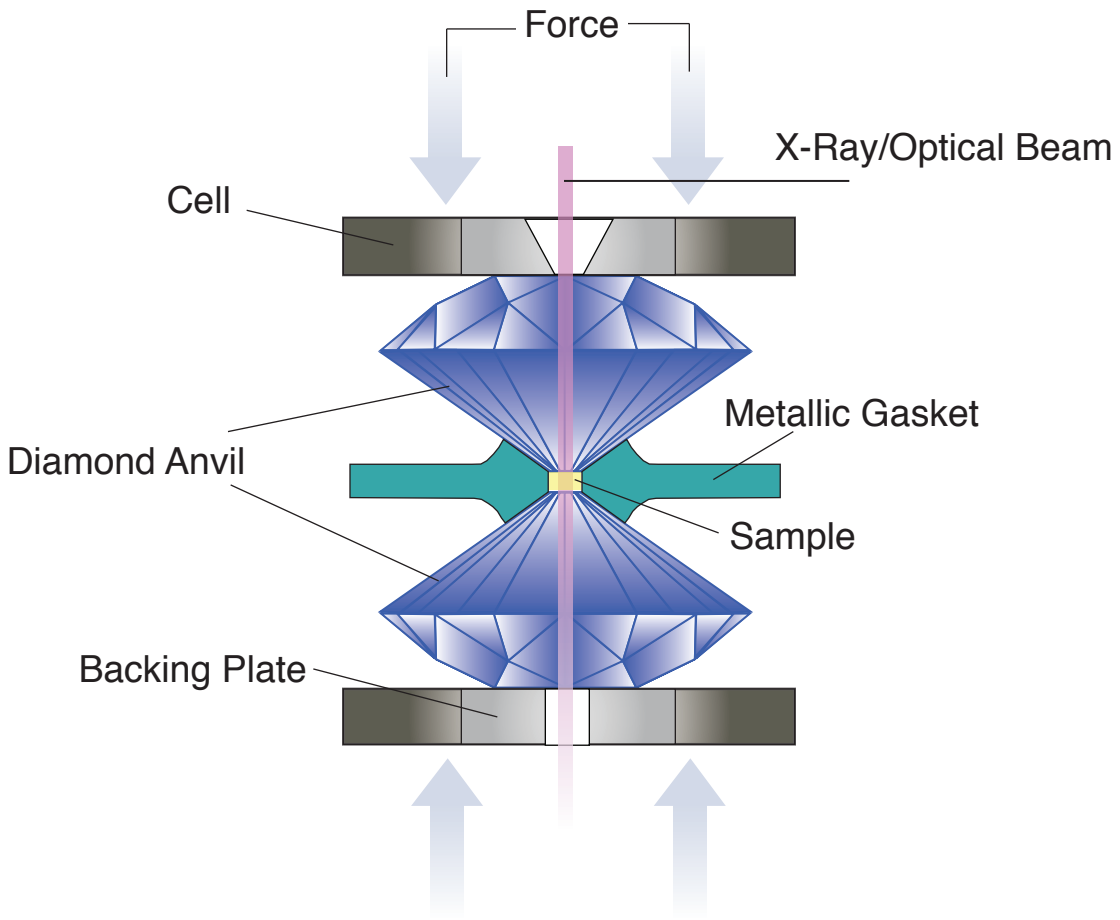

Figure 7.1: Schematic representation of a Diamond Anvil Cell

$P = (\lambda_{ruby} - \lambda_{ambientruby})/0.365$ as in Ref. 76. The ambient pressure values ($\lambda_{ambient}$) were measured by a single grain of annealed ruby placed on a microscope slide. The final pressure was determined by the average of the results for pressure for the R_1 and R_2 peaks. The degree of spread in pressure in the diamond anvil cell was calculated by the standard deviation of the results for all ruby peaks for each pressure measurement.

7.3 Beamline 12.2.2 of the Advanced Light Source

Beamline 12.2.2 of the Advanced Light Source is a dedicated high pressure x-ray diffraction beamline. It is located on the storage ring 6 T superconducting bend magnet producing usable hard x-rays with energies between 5 and 35 keV. Obtaining x-ray diffraction at high pressure requires a significant amount of flux, and hence a synchrotron source, because the diamonds have a high amount of absorbance. There are two endstations of this beamline; of which, we used only endstation 1. Detection was done with a Mar3450 imaging plate. Further information can be found in Ref. 71. Whereas most bulk mineral samples require only a few seconds to minutes, these nanoparticle samples commonly required 20 minutes of acquisition time. This was due to the low nanoparticle concentrations required to preserve nanoscale effects and prevent sample agglomeration.

Chapter 8

Conclusion

A student once asked a wise man how he should think of the scientific theories of the day. The wise man paused for a long time and then replied, "Our theories of nature are as rungs on a never-ending ladder, from the long-forgotten past, to the living present, into the undreamt future."
Richard Feynman, Character of Physical Law, p. 172-173.

They listened. They argued. They resorted to mathematics... Terry Pratchet

8.1 Summary

In conclusion, these studies have demonstrated that the crystallographic nature and the nature of the internal strain of multiply-twinned silver nanoparticles can lead to interesting behavior varying with pressure and with size. Distortions that can be described as orthorhombic or rhombohedral have been observed and interpreted in the context of ideally described Dh and Ih silver multiply-twinned nanoparticles. We recognize that these are ensembles of imperfect particles, hence this x-ray diffraction is weighted by volume per particle of the samples studied herein. However, convincing pressure-dependent trends have been identified. These trends are statistically significant, these distortions are real,

the distortions continuously vary with pressure, they are size dependent, and the distortion is altered when a sample is exposed to oxidation. This is a unique investigation into the interplay of thermodynamics, surface energy, and strain energy.

Understanding this behavior of silver nanoparticles enables further probes of pressure environments in otherwise inaccessible environments such as the interior of hollow nanospheres. Hollow materials, and in particular nanomaterials, are often lightweight and strong thus excellent building materials. Investigation into the mechanical behavior of these particles is invaluable. Using the information gained about the pressure-dependent behavior of silver nanoparticles as a function of size, the mechanical properties of one grain thick hollow nanospheres were determined.

Interesting outstanding questions of the work presented here are: Is there a pressure at which these multiply-twinned particles will convert to another structure? Is there a discrete transition at which one morphology is favored over another or will there always be overlap? What is the relative compressibility of these particles assuming these types of distortion? Further investigations in these structure and other similar noble metal nanoparticle structures are warranted.

8.2 The Impact Factor

Nanomaterials are most interesting for their technological relevance. For example, nanocrystalline materials have been long expected to have immense societal impact in the engineering of advanced building materials, in biological applications such as cancer remedies and biological probes, and in energy relevant applications such as batteries and solar

cells. The present study provides an example of the kind of science needed to extend these applications into extreme environments. For example, though the present study may have little implication in the technological arena, there is significant concern in environments where applications of silver nanoparticles are subject to extreme pressures. Some examples of these may be in cancer cells where large agglomerated cell masses can have forces up to nano-Newtons and in catalytic applications where materials for catalysis may be subjected to extreme pressures and temperatures. These studies suggest that silver nanoparticles in those extreme environments will not maintain the zero-pressure structure. Thus, looking at pressure effects could help in designing new nanosized objects with specific properties.

On a fundamental level, these studies have a significant impact on the understanding of the thermodynamic behavior of the morphology of noble metal nanoparticles. Though it has been established for over a decade that semiconductor nanoparticles[9] have size-dependent thermodynamic behavior few studies have indicated that noble metal nanoparticles might also have size-dependent thermodynamic behavior. Presssure-induced phase transitions are not common in bulk noble metals unless subject to extremely high pressure (on the order of 100s of GPa). These studies, however, show that this behavior is not maintained as the particle size becomes small, and thus dominated by surface. The present studies show that fundamentally unique pressure-dependent behaviors are observed for silver noble metal nanoparticles of varying morphology.

Bibliography

[1] M. Eremets, *High Pressure Experimental Methods*, (Oxford Science Publications, 1996)

[2] Y. Akahama, H. Kawamura, and A. K. Singh, J. Appl. Phys. **95**, 4767 (2004).

[3] A. Dewaele, P. Loubeyre, and M. Mezouar, Phys. Rev. B **70**, 094112 (2004).

[4] R.M. Hough, R.R.P. Noble, G.J. Hitchen, R. Hart, S.M. Reddy3 M. Saunders, P. Clode, D. Vaughan, J. Lowe, D.J. Gray, R.R. Anand, C.R.M. Butt and M. Verrall, Geology, **36**, 571, (2008).

[5] T. M. Benn, and P. Westerhoff, Environ. Sci. Technol **42** 4133 (2008)

[6] M. Takagi, J Phys. Soc. Jpn., **9**, 359 (1954).

[7] T. Castro, R. Reifenberger, E. Choi, and R. P. Andres, Phys. Rev. B **42** 8548 (1990).

[8] I. Shyjumon, M. Gopinadhan, O. Ivanova, M. Quaas, H. Wulff, C. A. Helm, and R. Hippler, Eur. Phys. J. D **37**, 409 (2005).

[9] S.H. Tolbert and A.P. Alivisatos, Science. **265** 373 (1994).

[10] K. Jacobs, D.J. Zaziski, E.C. Sher, A.B. Herhold, and A.P. Alivisatos, Science **293** 1803 (2001).

[11] J. N. Wickham, A.B. Herhold, and A.P. Alivisatos, Phys. Rev. Lett. **84** 923 (2000).

[12] S.M. Clark, S.G. Prilliman, C.K. Erdonmez, and A.P. Alivisatos, Nanotech., **16**, 2813 (2005).

[13] A. San-Miguel, Chem. Soc. Rev., **35**, 876 (2006).

[14] Y. Yin, C.K. Erdonmez, A. Cabot, S. Hughes, A.P. Alivisatos, Adv. Func. Mater. 16 1389 (2006)

[15] Y. Yin, R. M. Rioux, C.K. Erdonmez, S. Hughes, G.A. Samorjai, A.P. Alivisatos, 304, 714 (2004)

[16] D. Smigelskas, E. O. Kirkendall, TAIME, 171, 130, (1947)

[17] J. M. Buriak, Science, 304, 692 (2004)

[18] A. Cabot, R. K. Smith, Y. Yin, H. Zheng, B. M. Reinhard, H. Liu and A. P. Alivisatos. ACS Nano. **2**, 1452 (2008).

[19] A. Cabot, V. F. Puntes, E. Shevchenko, Y. Yin, L. Balcells, M. A. Marcus, S. M. Hughes, and A. P. Alivisatos. J. Am. Chem. Soc. **129**, 10358 (2007).

[20] L. D. Marks, Rep. Prog. Phys. **57**, 603 (1994).

[21] S. Ino, J. Phys. Soc. Jpn. **27** 941 (1969).

[22] L. D. Marks and D. Smith, J. Cryst. Growth **54**, 433 (1981).

[23] L. D. Marks and D. Smith, J. Microsc. **130**, 249C (1982).

[24] D. Reinhard, B. D. Hall, D. Ugarte, and R. Monot, Phys. Rev. B **55**, 7868 (1997).

[25] S. Ino and D. Ogawa, J. Phys. Soc. Jpn. **22** 1365 (1967).

[26] S. Ino, J. Phys. Soc. Jpn. **27** 346 (1967).

[27] M. J. Yacamán, J. A. Ascencio, H. B. Liu, and J. Gardea-Torresdey, J. Vac. Sci. Technol. B **19**, 1091 (2001).

[28] A. Howie and L. D. Marks, Philos. Mag. A, **49**, 95 (1984).

[29] S. Ino, J. Phys. Soc. Jpn. **21** 346 (1966).

[30] R. De Wit, J. Phys. C, **5**, 529 (1972).

[31] L. D. Marks and A. Howie, Nature, **282**, 196 (1979).

[32] Y. Saito, S. Yatsuya, K. Mihama, R. Uyeda, Jpn. J. Appl. Phys., **17**, 1149 (1978).

[33] B. G. Bagley, Nature **208**, 674 (1965).

[34] K. Heinemann, M. J. Yacaman, C. Y. Yang, and H. Poppa, J. Cryst. Growth, **47**, 177 (1979).

[35] C. Y. Yang, J. Cryst. Growth **47**, 274 (1979).

[36] V. G. Gryaznov and L. I. Trusov, Prog. Mater. Sci. **37**, 289 (1993).

[37] F. Silly and M. R. Castell, Appl. Phys. Lett. **87**, 213107 (2005).

[38] M. A Garcia-Pinilla, E. Perez-Tijerina, J. A. Garcia, C. Fernandez-Navarro, A. Tlahuice-Flores, S. Mejia-Rosales, J. M. Montejano-Carrizales, M. Jose-Yacaman, J. Phys. Chem. C **112** 13492, (2008).

[39] M. N. Blom, D. Schoos, J. Stairs, and M. M. Kappes, J. Chem. Phys. **124** 244308 (2006).

[40] X. Xing, R. M. Danell, I. L. Garzón, K. Michaelian, M. N. Blom, M. M. Burns, and J. H. Parks, Phys. Rev. B **72**, 081405(R) (2005).

[41] B. D. Hall, M. Fluëli, R. Monot, and J.-P. Borel, Phys. Rev. B **43**, 3906 (1991).

[42] B. D. Hall, D. Ugarte, D. Reinhard, and R. Monot, J. Chem. Phys. **103**, 2384 (1995).

[43] F. Baletto, R. Ferrando, Rev. Mod. Phys. **77**, 371 (2005).

[44] K. Sato, W. J. Huang, F. Bohra, S. Sivaramakrishnan, A. P. Tedjasaputra, and J. M. Zuo, Phys. Rev. B, **76** 144113 (2007).

[45] F. Baletto, C. Mottet, R. Ferrando, Phys. Rev. Lett. **84**, 5544 (2000).

[46] F. Baletto, C. Mottet, R. Ferrando, Phys. Rev. B **63**, 155408 (2001).

[47] X. Yang, W. Cai, and X. Shao, J. Phys. Chem. A **111**, 5048 (2007).

[48] F. Baletto, R. Ferrando, A. Fortunelli, F. Montalenti, and C. Mottet, J. Chem. Phys. **116**, 3856 (2002).

[49] K. Koga, K. Sugawara, Surf. Sci. **529** 23 (2003).

[50] Q. F. Gu, G. Krauss, F. Gramm, A. Cervellino, and W. Steurer, Phys. Rev. Lett. **100**, 045502 (2008).

[51] Calvo and Doye, Phys Rev. B **69** 12514 (2005).

[52] G.C. Kennedy and R.N. Keeler, in American Institute of Physics Handbook, 3rd ed. (McGraw-Hill, New York, 1972), Sec. 4. p. 101.

[53] W. J. Carter, S.P. Marsh, J.N. Fritz, and R.G. McQueen, in Accurate Characterization of the High Pressure Environment, edited by E.C. Lloyed (U.S. GPA, Washington DC, 19971), pp 189-200.

[54] J. Xie, S.P. Chen, S. Gironcoli, and S. Baroni, Philos. Mag. B, **79**. 911 (1999).

[55] K. Syassen and W. B. Holzapfel, J. Appl. Phys. 49, 4427 (1978).

[56] P.I. Dorogokupets and A. P. Oganov, Doklady Earth Sciences. **391A**, 854 (2003).

[57] L. Liu, and W. A. Bassett, J. Appl. Phys. **44** 1475 (1973).

[58] S. N. Vaidya and G. C. Kennedy, J. Phys. Chem. Solids, **31**, 2329, (1970).

[59] W. B. Daniels and C. S. Smith, Phys. Rev. **111**, 713 (1958).

[60] P. S. Ho, J. P. Poirier, and A. L. Ruoff, Phys. Stat. Sol. **35**, 1017 (1969).

[61] Y. Hiki and A. V. Granato, Phys. Ref. **144**, 411 (1966).

[62] C. L. Johnson, E. Snoek, M. Ezcurdia, B. Rodríguez-González, I. Pastoriza-Santos, L. M. Liz-Marzán, and M. J. Hÿtch, Nature Mater. **7**, 120 (2008).

[63] V. G. Gryaznov, J. Heydenreich, A. M. Kaprelov, S. A. Nepijko, A. E. Romanov, and J. Urban, Cryst. Res. Technol. **34**, 1091 (1999).

[64] Y. Tang and M. Ouyang, Nature Mater. **6**, 754 (2007).

[65] C. Mohr, H. Hofmeister, and P. Claus, J. Catal. **213**, 86 (2003).

[66] G. C. Kennedy and R. N. Keeler, *American Institute of Physics Handbook*, 3rd ed. (McGraw-Hill, New York, 1972), Sec. 4 p. 101.

[67] K. S. Suslick, M. Fang, and T. Hyeon, J. Am. Chem. Soc. **118**, 11960 (1996).

[68] M. Green, Chem. Commun. (Cambridge) 2005, 3002.

[69] Y. Yin, C. Erdonmez, S. Aloni, and A. P. Alivisatos, J. Am. Chem. Soc. **128**, 12671 (2006).

[70] N. S. Sobal, U. Ebels, H. Möhwald, and M. Giersig, J. Phys. Chem. B **107** 7351 (2003).

[71] M. Kunz, A. A. MacDowell, Wendel A Caldwell, D Cambie, R. S. Celestre, E. E. Domning, R. M. Duarte, A. E. Gleason, J. M. Glossinger, N. Kelez, D. W. Plate, T. Yu, J. M. Zaug, H. A. Padmore, R. Jeanloz, A. P. Alivisatos, and S. M. Clark, J. Synchrotron Radiat. **12**, 650 (2005).

[72] A. P. Hammersley, ESRF Internal Report No. ESRF98HA01T, FIT2D, V9.129 Reference Manual V3.1, 1998 (unpublished)

[73] W. F. Oliver, C. A. Herbst, and G. H. Wolf, J. Non-Cryst. Solids **131-133**, 84 (1991)

[74] G. J. Piermarini, S. Block and J. D. Barnett, J. Appl. Phys. **44**, 5377 (1973)

[75] K. Jacobs, D. Zaziski, E. C. Scher, A. B. Herhold, and A. P. Alivisatos, J. Phys. Chem. B **106**, 3759 (2002).

[76] G. J. Piermarini, S. Block, J. D. Barnett, and R. A. Forman, J. Appl. Phys. **46**, 2774 (1975).

[77] H. K. Mao, P. M. Bell, J. W. Shaner, and D. J. Steinberg, J. Appl. Phys. **49**, 3276 (1978).

[78] P. Vinet, J. H. Rose, J. Ferrante, and J. R. Smith, J. Phys.: Condens. Matter **1**, 1941 (1989).

[79] R. F. S. Hearmon, Rev. Mod. Phys. **18**, 409 (1946).

[80] R. Bacon and C. S. Smith, Acta Metall. **4**, 337 (1956).

[81] J. R. Neighbours and G. A. Alers, Phys. Rev. **111**, 707 (1958).

[82] K. N. Khanna, Solid State Commun. **29**, 801 (1979).

[83] P. Mahazzabi, J. Phys. Chem. **46**, 147 (1985).

[84] A. Wolfenden and M. R. Harmouche, J. Mater. Sci. **28**, 1015 (1993).

[85] J. F. Nye, *Physical Properties of Crystals*. (Clarendon, Oxford, UK, 1957), pp. 144-145.

[86] W. M. Moore and P. J. Codella, J. Phys. Chem. **92**, 4421 (1988).

[87] S. Krüger, S. Vent, F. Nortemann, M. Staufer, and N. Rösch, J. Chem. Phys. **115**, 2082 (2001).

[88] Q. Guo, Y. Zhao, W. L. Mao, Z. Wang, Y. Xiong, and Y. Xia, Nano Lett. **8**, 972 (2008).

[89] L. Miyagi, S. Merkel, T. Yagi, N. Sata, Y. Ohishi, and H,-R. Wenk, J. Phys.: Condens. Matter **18**, S995 (2006).

[90] G. Ischia, H-R. Wenk, L. Lutterotti, and F. Berberich, J. Appl. Crystallogr. **38**, 37 (2005).

[91] A. L. Mackay, Acta Crystallogr. **15**, 916 (1962).

[92] http://www.jmol.org

[93] C. Solliard and M. Flueli, Surf. Sci. **156**, 487 (1985).

[94] B. Raoult, J. Farges, M. F. De Feraudy, and G. Torchet, Philos. Mag. B **60**, 881 (1989).

[95] X. Ren, X. Meng, D. Chen, F. Tang, and J. Jiao, Biosensors and Bioelectronics, **21**, 433 (2005).

[96] C. Sönnichsen, B. M. Reinhard, J. Liphardt, and A. P. Alivisatos, Nature Biotech, **23**, 741 (2005)

[97] A. R. Shahverdi, A. F. Fakhimi, H. R. Shahverdi, S. Minaian, Nanomedicine; Nanotechnology, Biology, and Medicine, **3**, 168, (2007)

[98] C. Solliard, Surf. Sci. **106**, 58 (1981).

[99] K.J. Koski, N.M. Kamp, R.K. Smith, M. Kunz, J.K. Knight, A.P. Alivisatos, Phys. Rev. B **78**, 165410 (2008).

[100] Z. W. Shan, G. Adesso, A. Cabot, M. P. Sherburne, S. A. Syed Asif, O. L. Warren, D. C. Chrzan, A. M. Minor, and A. P. Alivisatos, Nat. Mater. **7** 947 (2008).

[101] Y.-T. Cheng, C.-M. Cheng, Mater. Sci. and Eng. R, **44**, 91, 2004.

[102] Y. Sun, B. Mayers, Y. Xia, Adv. Mater., **15** 641 (2003).

[103] Y. Xia and J. Chen, Agnew. Chem. 117, 2645, (2005).

[104] S. Maksimuk, X. Teng, and H. Yang, Phys. Chem. Chem. Phys., **8**, 4660, 2006.

[105] E. V. Shevchenko, M. I. Bodnarchuk, M. V. Kovalenko, D. V. Talapin, R. K. Smith, S. Aloni, W.Heiss, and A. P. Alivisatos, Adv. Mater. **9999**, 1 (2008).

[106] H. J. Fan, U. Gösele, and M. Zacharias, Small **3**, 1660, (2007).

[107] B. Jiang and G.J. Weng, Int. J. of Plasticity **20** 2007, (2004).

[108] Y. Cui, M. T. Bjork, J. A. Liddle, C. Sonnichsen, B. Boussert, A. P. Alivisatos, Nano Lett. **4** 1093, (2004)

[109] Y. Cui, U. Banin, M. T. Bjork, A. P. Alivisatos, Nano Lett. **5** 1519, (2005).

[110] P. -E. Trudeau, M. Sheldon, V. Altoe, A. P. Alivisatos, Nano Lett. **8** 1936 (2008).

[111] A. Jayaraman, Rev. Sci. Instr., **57** 1013, (1986).

Appendix A

Appendix A: Pressure Gradient Across a Hollow Nanoshell

For our particular problem, we want to find what the pressure gradient across the shell of a hollow sphere will be if we apply an external pressure. To do this we need to evaluate the stress state of the hollow sphere via the mechanical properties of the material of the hollow shell. For this to be relevant in determining a useful parameter particular to the mechanical properties of the hollow nanosphere, this derivation aims at relating the pressure gradient across a hollow shell to the yield strength of the hollow nanoparticle.

The definition of stress is the force per area on a surface with a unit normal j and is given by

$$\sigma_{ijhj} = f_i \tag{A.1}$$

where

$$\sum_{j=1}^{3} \sigma_{ijhj} \rightarrow vector \tag{A.2}$$

We want to find what the net force will be on our shell in our particular problem. To do this we can look at the sum of forces on an elemental voxel representing a cutout of our hollow sphere as is shown in the figure below. This may be a bit confusing because I have two $d\theta$ but in our spherical symmetric case we can assume that $d\phi = d\theta$ because a sphere of a cubic material under hydrostatic pressure will remain a sphere.

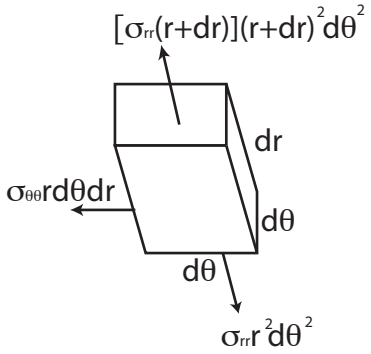

As is shown in the figure, the net force overall will be in the radial direction because everything else (for example the θ components of all of the forces on the sides in this voxel) cancels from symmetry. What we get then is:

$$\sum_{i} f_i = \sigma_{\theta\theta} r d\theta dr (sin\frac{\theta}{2}) \rightarrow \sigma_{\theta\theta} r d\theta dr \frac{d\theta}{2} \tag{A.3}$$

Assuming that θ is small, $sin\frac{\theta}{2} = \frac{\theta}{2}$. Our stress tensor for this system then is:

$$\vec{\sigma} = \begin{bmatrix} \sigma_{\theta\theta} & 0 & 0 \\ 0 & \sigma_{\theta\theta} & 0 \\ 0 & 0 & \sigma_{rr} \end{bmatrix} \tag{A.4}$$

Now we need to add it all up! First, we can expand $\sigma_{rr}(r + dr)$ as:

$$\sigma_{rr}(r + dr) = \sigma_{rr} + \sigma_{rr,r}dr + ... \tag{A.5}$$

Then the sum of forces is:

$$\sum f_i = (\sigma_{rr} + \sigma_{rr,r}dr)(r + dr)^2 d\theta^2 - \sigma_{rr}r^2 d\theta^2 - 4\left[\sigma_{\theta\theta} r d\theta dr \frac{d\theta}{2}\right] \tag{A.6}$$

We should only keep the 1st nonvanishing term and get rid of all higher 2nd and 3rd order terms because they aren't going to impact our solution much. Simplifiying:

$$\sum f_i = \left[\sigma_{rr}r^2 + 2\sigma_{rr}rdr + \sigma_{rr}dr^2 + \sigma_{rr,r}r^2 dr + 2\sigma_{rr,r}rdr^2 + \sigma_{rr,r}dr^3\right] d\theta^2 - \sigma_{rr}d\theta^2 r^2 - 4\left[\sigma_{\theta\theta} r d\theta dr \frac{d\theta}{2}\right] \tag{A.7}$$

$$\sum f_i = \left[2\sigma_{rr}rdr + \sigma_{rr,r}r^2 dr\right] d\theta^2 - 2\left[\sigma_{\theta\theta} r dr d\theta^2\right] \tag{A.8}$$

$$\sum f_i = 2\sigma_{rr}rdrd\theta^2 + \sigma_{rr,r}r^2 drd\theta^2 - 2\sigma_{\theta\theta}rdrd\theta^2 \tag{A.9}$$

The sum of the forces is zero in a static equilibrium case so we can get rid of an $rdrd\theta^2$ and we have the equation for the net force in the static pressure case:

$$\sum f_i = 2\sigma_{rr} + r\sigma_{rr,r} - 2\sigma_{\theta\theta} = 0 \tag{A.10}$$

Next, we need to find the strain, ϵ across the shell. The definition of strain in the linear, nonisotropic case is:

$$\epsilon_{ij} = \frac{1}{2}\left[\frac{\partial u_i}{\partial x_j} + \frac{\partial u_j}{\partial x_i}\right] \tag{A.11}$$

Strain is 1/2 the sum of the gradient of the displacements.

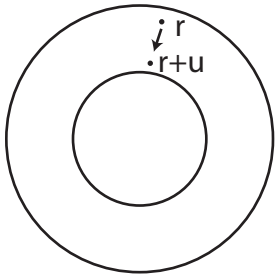

In spherical coordinates, the only displacement is in the radial direction. Figure 2 shows a picture of this to help find our strain coordinates. If we have a point, r, in the sphere it displaces from $r \rightarrow r - u$ and the circumference of the sphere will go from $2\pi r \rightarrow 2\pi(r-u)$ when we apply a pressure this means that the strain in the radial direction, r is $\epsilon_{rr} = \frac{du}{dr}$ and the strain in the θ direction is $\epsilon_{\theta\theta} = -\frac{u}{r}$.

Thus our strain tensor for this system is:

$$\epsilon_{ij} = \begin{bmatrix} -\frac{u}{r} & 0 & 0 \\ 0 & -\frac{u}{r} & 0 \\ 0 & 0 & -\frac{du}{dr} \end{bmatrix} \tag{A.12}$$

Now we need to find the connection between stress and strain. In a Cartesian coordinate system this is:

$$\epsilon_{xx} = \frac{\sigma_{xx}}{E} \quad \epsilon_{yy} = -\frac{\sigma_{xx}\nu}{E} = \epsilon_{zz} \tag{A.13}$$

But we're using a spherical coordinate system, so this is just:

$$\epsilon_{rr} = \frac{\sigma_{rr}}{E} - \frac{2\nu\sigma_{\theta\theta}}{E} \quad \epsilon_{\theta\theta} = \frac{\sigma_{\theta\theta}}{E} - \frac{\sigma_{rr}\nu}{E} - \frac{\nu\sigma_{\theta\theta}}{E} \tag{A.14}$$

$$\epsilon_{rr} = \frac{\sigma_{rr}}{E} - \frac{2\nu\sigma_{\theta\theta}}{E} = \frac{u}{r} \quad \epsilon_{\theta\theta} = \frac{\sigma_{\theta\theta}}{E} - \frac{\sigma_{rr}\nu}{E} - \frac{\nu\sigma_{\theta\theta}}{E} = \frac{du}{dr} \tag{A.15}$$

If we solve, the above equation for $\sigma_{\theta\theta}$ and σ_{rr}, we find:

$$\sigma_{\theta\theta} = -\frac{E(u+r\nu u')}{2r\nu^2+r\nu-r} \quad \sigma_{rr} = -\frac{E(-2\nu u-ru'+r\nu u')}{2r\nu^2+r\nu-r} \tag{A.16}$$

We put this into our equation for the sum of the forces and then solve that differential equation for $u(r)$ and find the simple solution. This was done in Mathematica.:

$$u(r) = rC_1 + \frac{C_2}{r^2} \tag{A.17}$$

Where $C1$ and $C2$ are constants from solving the differential equation and can be found by applying boundary conditions. Something to notice is that this solution basically

has two parts. The first part is rC_1 and this is just the solution for uniform compression. The second part is $\frac{C_2}{r^2}$ and this is unique to the hollow sphere. If we had a solid sphere, this part would be zero, and we'd recover just uniform compression! (So the solution seems good!) Up until now all this is textbook. We're going to take a different approach from here on out by applying different boundary conditions than you might find elsewhere.

We apply the boundary conditions that at $r = a$, the inner radius, the pressure is Pa and at $r = b$, the outer radius of the hollow sphere, the pressures is Pb. When we apply this boundary conditions and solve for C_1 and C_2, we find:

$$C_1 = -\frac{(a^3Pa - b^3Pb)(2\nu - 1)}{(a^3 - b^3)E} \quad C_2 = \frac{a^3b^3(Pa - Pb)(1+\nu)}{2(a^3 - b^3)E} \tag{A.18}$$

Since C_1 doesn't contribute to the shear stress in the hollow sphere, for the purpose of finding the maximum shear stress, we can set $C_1 = 0$. Now we need to find σ_{rr} and $\sigma_{\theta\theta}$ and calculate the maximum shear stress which is given by:

$$\tau_{max} = \frac{1}{3}\left[(\sigma_{rr} - \sigma_{\theta\theta})^2 + (\sigma_{rr} - \sigma_{\theta\theta})^2 + (\sigma_{\theta\theta} - \sigma_{\theta\theta})^2\right]^{\frac{1}{2}} \tag{A.19}$$

.

$$\sigma_{rr} = \frac{-2EC_2}{r^3(1+\nu)} \quad \sigma_{\theta\theta} = \frac{EC_2}{r^3(1+\nu)} \tag{A.20}$$

Something worth noticing at this point, if we substitute our expressions above for $\sigma_{\theta\theta}$ and σ_{rr} into the stress tensor, and find the trace, $Tr[\vec{\sigma}] = 0$ which means the pure shear case. (This makes sense.)

Solving for τ_{max} gives:

$$\tau_{max} = \sqrt{2}\sqrt{\frac{E^2 C_2^2}{r^6(1+\nu)^2}} \tag{A.21}$$

$$\tau_{max} = \left(\frac{1}{\sqrt{2}}\right)\frac{a^3 b^3 |Pa - Pb|}{|a^3 - b^3| r^3} \tag{A.22}$$

Since $b > a$, this means that $|a^3 - b^3| = b^3 - a^3$ so we can drop the absolute value sign using $(b^3 - a^3)$ and evaluating at $r = a$:

$$\tau_{max} = \frac{b^3 |Pa - Pb|}{\sqrt{2}(b^3 - a^3)} \tag{A.23}$$

And evaluating at $r = b$:

$$\tau_{max} = \frac{a^3 |Pa - Pb|}{\sqrt{2}(b^3 - a^3)} \tag{A.24}$$

Since, the larger τ_{max} is at $r = a$, we can now use the solution for the maximum shear stress (which is the maximum shear strength, Y and also called the yield strength) to find the pressure gradient across our hollow sphere:

$$|Pa - Pb| = Y\left(\frac{\sqrt{2}(b^3 - a^3)}{b^3}\right) = Y\sqrt{2}\left(1 - \frac{a^3}{b^3}\right) \tag{A.25}$$

It makes sense that we have to have absolute value signs around Pa-Pb because the pressure gradient could go either way.

Roughly shear strengths are on the order of 100 MPa to 700 MPa. This however depends on the grain size in the material. For a nanomaterial we will have high shear strengths but we cannot say for certain how great that number will be.

DISCLAIMER